



**Calhoun: The NPS Institutional Archive**  
**DSpace Repository**

---

Theses and Dissertations

1. Thesis and Dissertation Collection, all items

---

2017-12

Field ionization test chamber for carbon  
nanotube-based miniature ion thruster applications

Crosby, Bryan D.

Monterey, California: Naval Postgraduate School

---

<http://hdl.handle.net/10945/56899>

*Downloaded from NPS Archive: Calhoun*



Calhoun is a project of the Dudley Knox Library at NPS, furthering the precepts and goals of open government and government transparency. All information contained herein has been approved for release by the NPS Public Affairs Officer.

**Dudley Knox Library / Naval Postgraduate School**  
**411 Dyer Road / 1 University Circle**  
**Monterey, California USA 93943**

<http://www.nps.edu/library>



**NAVAL  
POSTGRADUATE  
SCHOOL**

**MONTEREY, CALIFORNIA**

**THESIS**

**FIELD IONIZATION TEST CHAMBER FOR CARBON  
NANOTUBE-BASED MINIATURE ION THRUSTER  
APPLICATIONS**

by

Bryan D. Crosby

December 2017

Thesis Advisor:

Dragoslav Grbovic

Co-Advisor:

Oscar Biblarz

**Approved for public release. Distribution is unlimited.**

*Reissued 27 Sep 2018 to reflect updated abstract on pages i and v.*

THIS PAGE INTENTIONALLY LEFT BLANK

REPORT DOCUMENTATION PAGE			Form Approved OMB No. 0704-0188	
Public reporting burden for this collection of information is estimated to average 1 hour per response, including the time for reviewing instruction, searching existing data sources, gathering and maintaining the data needed, and completing and reviewing the collection of information. Send comments regarding this burden estimate or any other aspect of this collection of information, including suggestions for reducing this burden, to Washington headquarters Services, Directorate for Information Operations and Reports, 1215 Jefferson Davis Highway, Suite 1204, Arlington, VA 22202-4302, and to the Office of Management and Budget, Paperwork Reduction Project (0704-0188) Washington, DC 20503.				
<b>1. AGENCY USE ONLY</b> <i>(Leave blank)</i>	<b>2. REPORT DATE</b> December 2017	<b>3. REPORT TYPE AND DATES COVERED</b> Master's thesis		
<b>4. TITLE AND SUBTITLE</b> FIELD IONIZATION TEST CHAMBER FOR CARBON NANOTUBE-BASED MINIATURE ION THRUSTER APPLICATIONS			<b>5. FUNDING NUMBERS</b>	
<b>6. AUTHOR(S)</b> Bryan D. Crosby				
<b>7. PERFORMING ORGANIZATION NAME(S) AND ADDRESS(ES)</b> Naval Postgraduate School Monterey, CA 93943-5000			<b>8. PERFORMING ORGANIZATION REPORT NUMBER</b>	
<b>9. SPONSORING /MONITORING AGENCY NAME(S) AND ADDRESS(ES)</b> N/A			<b>10. SPONSORING / MONITORING AGENCY REPORT NUMBER</b>	
<b>11. SUPPLEMENTARY NOTES</b> The views expressed in this thesis are those of the author and do not reflect the official policy or position of the Department of Defense or the U.S. Government. IRB number ___N/A___.				
<b>12a. DISTRIBUTION / AVAILABILITY STATEMENT</b> Approved for public release. Distribution is unlimited.			<b>12b. DISTRIBUTION CODE</b> A	
<b>13. ABSTRACT</b>  <p>Electric propulsion for micro- and nano-satellites is an increasingly viable solution for station keeping and end-of-life operations. In particular, microelectromechanical systems electrodes for use in a field ionization electric propulsion thruster are starting to show promise as a viable plasma generator electrode. This was determined by utilizing a bell jar pressure chamber and a proof-of-concept field ionization electrode characterization fixture complete with an accelerator mesh grid, as well as a beam current data acquisition suite. The complete field ionization electrode characterization apparatus enables the user to view the generated ion plasma and collect beam current and enables future work to incorporate a thrust stand and a cathode/anode gap micrometer.</p> <p>Beam current collected from a series of experiments comparing angled-wall etched nozzles with and without carbon nanotube (CNT) deposition showed a distinct improvement in maximum collected current. Mass utilization efficiency and specific impulse for a CNT electrode were found to be 0.31% and 17.5 seconds, respectively, at 560V. This is marginal in comparison to thrusters in industry; however, it shows a successful apparatus and test fixture proof of concept.</p>				
<b>14. SUBJECT TERMS</b> carbon nanotubes, field emission, field ionization, electrostatic ion propulsion, cubesat			<b>15. NUMBER OF PAGES</b> 87	
			<b>16. PRICE CODE</b>	
<b>17. SECURITY CLASSIFICATION OF REPORT</b> Unclassified	<b>18. SECURITY CLASSIFICATION OF THIS PAGE</b> Unclassified	<b>19. SECURITY CLASSIFICATION OF ABSTRACT</b> Unclassified	<b>20. LIMITATION OF ABSTRACT</b> UU	

THIS PAGE INTENTIONALLY LEFT BLANK

**Approved for public release. Distribution is unlimited.**

**FIELD IONIZATION TEST CHAMBER FOR CARBON NANOTUBE-BASED  
MINIATURE ION THRUSTER APPLICATIONS**

Bryan D. Crosby  
Lieutenant, United States Navy  
B.S., Ohio University, 2010

Submitted in partial fulfillment of the  
requirements for the degree of

**MASTER OF SCIENCE IN APPLIED PHYSICS**

from the

**NAVAL POSTGRADUATE SCHOOL  
December 2017**

Approved by: Dr. Dragoslav Grbovic  
Thesis Advisor

Dr. Oscar Biblarz  
Co-Advisor

Dr. Kevin Smith  
Chair, Department of Physics

THIS PAGE INTENTIONALLY LEFT BLANK

## ABSTRACT

Electric propulsion for micro- and nano-satellites is an increasingly viable solution for station keeping and end-of-life operations. In particular, microelectromechanical systems electrodes for use in a field ionization electric propulsion thruster are starting to show promise as a viable plasma generator electrode. This was determined by utilizing a bell jar pressure chamber and a proof-of-concept field ionization electrode characterization fixture complete with an accelerator mesh grid, as well as a beam current data acquisition suite. The complete field ionization electrode characterization apparatus enables the user to view the generated ion plasma and collect beam current and enables future work to incorporate a thrust stand and a cathode/anode gap micrometer.

Beam current collected from a series of experiments comparing angled-wall etched nozzles with and without carbon nanotube (CNT) deposition showed a distinct improvement in maximum collected current. Mass utilization efficiency and specific impulse for a CNT electrode were found to be 0.31% and 17.5 seconds, respectively, at 560V. This is marginal in comparison to thrusters in industry; however, it shows a successful apparatus and test fixture proof of concept.

THIS PAGE INTENTIONALLY LEFT BLANK

# TABLE OF CONTENTS

<b>I.</b>	<b>INTRODUCTION.....</b>	<b>1</b>
<b>II.</b>	<b>BACKGROUND .....</b>	<b>5</b>
<b>A.</b>	<b>PRINCIPLES OF ION THRUSTER ELECTRIC PROPULSION .....</b>	<b>5</b>
	1. Ion Thruster Design.....	7
	2. Ionization Methods .....	9
<b>B.</b>	<b>FIELD EMISSION AND FIELD IONIZATION.....</b>	<b>10</b>
	1. Field Emission .....	10
	2. Field Ionization.....	14
<b>C.</b>	<b>CARBON NANOTUBE ELECTRODES FOR FIELD IONIZATION.....</b>	<b>17</b>
	1. Angled-Wall Etched CNTs.....	18
	2. Nano-Scribed Micro-Pillar Array Nozzle.....	19
<b>D.</b>	<b>FIELD IONIZATION TEST CHAMBER .....</b>	<b>19</b>
	1. Limitations of Previous Test Chamber Generations .....	20
	2. Fourth-Generation Test Chamber Objectives .....	20
<b>III.</b>	<b>EXPERIMENTAL APPARATUS.....</b>	<b>23</b>
<b>A.</b>	<b>DESIGN OF THE FOURTH-GENERATION TEST CHAMBER.....</b>	<b>23</b>
	1. Vacuum Chamber (Bell Jar) Construction .....	24
	2. Field Ionization Test Apparatus .....	25
	3. Mass Flow Controller and Argon Gas Injection System.....	28
	4. High Voltage Source and Current Measurement Apparatus .....	30
	5. Thrust Measurement Apparatus .....	30
<b>B.</b>	<b>EXPERIMENTAL METHODS .....</b>	<b>31</b>
<b>IV.</b>	<b>EXPERIMENTAL RESULTS.....</b>	<b>33</b>
<b>A.</b>	<b>FIELD IONIZATION RESULTS .....</b>	<b>33</b>
<b>B.</b>	<b>EXPERIMENTAL THRUST .....</b>	<b>42</b>
<b>V.</b>	<b>CONCLUSION AND RECOMMENDATIONS.....</b>	<b>45</b>
<b>A.</b>	<b>SUMMARY AND CONCLUSIONS .....</b>	<b>45</b>
<b>B.</b>	<b>FUTURE WORK AND RECOMMENDATIONS .....</b>	<b>45</b>
	1. Field Ionization Test Apparatus .....	45

2.	Carbon Nanotube Electrodes.....	47
3.	Plasma Generator and Accelerator Mesh Grid .....	47
4.	Field Ionization Electric Propulsion Geometry .....	48
5.	Characterization of Thrust and Plasma Plume .....	48
APPENDIX A. COMPUTER-AIDED DESIGN.....		49
APPENDIX B. RAW THRUST DATA.....		51
APPENDIX C. MATLAB CODE.....		55
APPENDIX D. ADDITIONAL IMAGES.....		57
APPENDIX E. EXPERIMENTAL LOG.....		61
LIST OF REFERENCES .....		63
INITIAL DISTRIBUTION LIST .....		67

## LIST OF FIGURES

Figure 1.	OUTSat mated to centaur stage of the NROL-36 mission. Adapted from [2].	2
Figure 2.	Cluster of ENPULSION IFM-350 FEEP thrusters. Source: [10].	4
Figure 3.	Simplified schematic diagram of an electron bombardment ion thruster. Source: [1].	7
Figure 4.	Simplified 1-D view of a three-grid accelerator system. Source: [11].	8
Figure 5.	Field emission model potential well schematic.	11
Figure 6.	FN plot of an unpolished copper substrate with an electrode gap of 500 $\mu$ m. Source: [18].	13
Figure 7.	FN plot of selected samples. Source: [17].	13
Figure 8.	Field ionization model potential well schematic showing the Coulombic barrier (a) and the distorted potential well by the application of an electrical potential (b). Source: [19].	14
Figure 9.	SEM micrograph: Nozzle cross-section after CNT growth. Source: [23].	18
Figure 10.	SEM micrograph of the nano-scribed micro-pillar array nozzle from ORNL.	19
Figure 11.	Block diagram of the FI test apparatus and the High Voltage–Current Measure DaQ suite.	23
Figure 12.	3D CAD representation of the Bell Jar vacuum chamber and plasma generator apparatus.	24
Figure 13.	3D CAD drawing of the FIEP experimental fixture.	25
Figure 14.	Plasma generator (left) and Accelerator Mesh Grid (right) PCBs post- experiment.	26
Figure 15.	3D CAD representation of the FI Test Fixture assembly.	27
Figure 16.	Expanded view of the FI Test Fixture assembly.	28
Figure 17.	Sierra Instruments Smart-Trak 2 Series 100 Mass Flow Controller. Source: [25].	29

Figure 18.	Flow paths through the Smart-Trak 2 Thermal Mass Flow Controller. Source: [25].	29
Figure 19.	Femto Tools FT-S100/1000 cantilever force gauge.	31
Figure 20.	Ion plasma visible during a beam current measurement experiment.	33
Figure 21.	Top: average Blank compared to average CNT at 3g/hr, 3 runs each; bottom: fresh Blank compared to fresh CNT at 3g/hr as compared to theoretical CL current.	34
Figure 22.	Townsend avalanche regimes.	36
Figure 23.	Top: Ion beam current versus voltage (multiple CNT runs at 3g/hr), bottom: Ion beam current versus voltage (multiple Blank runs at 3g/hr).	37
Figure 24.	Arcing through the FR4 substrate causing a failed experiment.	37
Figure 25.	SEM micrographs of an unused (A) and heavily used (B) APG2017_5 sample with CNT deposition.	38
Figure 26.	SEM micrographs of an unused (A) and heavily used (B) APG2017_5 Blank sample.	39
Figure 27.	Comparison of SEM micrographs of the AMG condition after a Fresh sample (A) and a heavily used sample experiment (B), (C) is a micrograph of an unused Copper mesh.	40
Figure 28.	1) MUF for fresh Blank compared to fresh CNT at 3g/hr, 2) $I_{sp}$ for fresh Blank compared to fresh CNT at 3g/hr, 3) Calculated Thrust for fresh Blank compared to fresh CNT at 3g/hr, 4) FIEP Power consumption.	41
Figure 29.	Top: Comparison of MUF to mass flow rate; bottom: beam current versus voltage at 0.5g/hr showing linear relationship below turn-on.	42
Figure 30.	Top: comparison of measured and calculated thrust; bottom: $I_{sp}$ from measured thrust (fresh CNT3).	43
Figure 31.	Printed Circuit Board electrode schematic (AutoDesk Eagle Software).	49
Figure 32.	2D drawing of the 3D printed experimental fixture.	50

Figure 33.	Raw thrust data for a fresh CNT sample at 2g/hr (FT-S1000 Gain: 496.6 $\mu\text{N/V}$ ).....	51
Figure 34.	Raw thrust data for the second run of a CNT sample at 2g/hr (FT-S1000 Gain: 496.6 $\mu\text{N/V}$ ).....	51
Figure 35.	Raw thrust data for the third run of a CNT sample at 2g/hr (FT-S1000 Gain: 496.6 $\mu\text{N/V}$ ).....	52
Figure 36.	Raw thrust data for a correction factor experiment at 2g/hr (FT-S1000 Gain: 496.6 $\mu\text{N/V}$ ).....	52
Figure 37.	Flow to No-Flow thrust experiments varying mass flow rate (FT-S1000 Gain: 496.6 $\mu\text{N/V}$ ).....	53
Figure 38.	Images showing the relative intensity of the ion plasma from a CNT sample—top: 450V Hold, middle: 500V Hold, bottom: 550V Hold.....	57
Figure 39.	FT-S1000 (Gain: 496.6 $\mu\text{N/V}$ ) cantilever force gauge placement in the plasma plume. ....	58
Figure 40.	FT-S1000 (Gain: 496.6 $\mu\text{N/V}$ ) cantilever force gauge correction factor experiment. ....	58
Figure 41.	Beam current versus voltage of the Blank sample (average of three experiments) and a fresh CNT sample varying mass flow rate. ....	59
Figure 42.	FIEP Experimental log.....	61

THIS PAGE INTENTIONALLY LEFT BLANK

**LIST OF TABLES**

Table 1. List of CubeSat micro-propulsion currently in industry. Adapted from [4]–[10]. .....3

THIS PAGE INTENTIONALLY LEFT BLANK

## LIST OF ACRONYMS AND ABBREVIATIONS

ABS	Acrylonitrile Butadiene Styrene
AMG	Accelerator Mesh Grid
CAD	Computer Aided Design
CL	Child – Langmuir
CNT	Carbon Nanotube
DaQ	Data Acquisition System
FE	Field Emission
FI	Field Ionization
FEEP	Field Emission Electric Propulsion
FIEP	Field Ionization Electric Propulsion
FN	Fowler-Nordheim
ISS	International Space Station
LEO	Low Earth Orbit
MEMS	Microelectromechanical Systems
NASA	National Aeronautics and Space Administration
NPS	Naval Postgraduate School
NPSCuL	Naval Postgraduate School CubeSat Launcher
NPT	National Pipe Thread
NRO	National Reconnaissance Office
ORNL	Oak Ridge National Laboratory
OUTSat	Operationally Unique Technologies Satellite
PCB	Printed Circuit Board
RTD	Resistance Temperature Detector
VLEO	Very Low Earth Orbit
WKB	Wentzel-Kramers-Brillouin

THIS PAGE INTENTIONALLY LEFT BLANK

## **ACKNOWLEDGMENTS**

This thesis is truly the product of a team effort. I could not have achieved so much without the help of so many great people. In particular, I would like to thank Dr. Dragoslav Grbovic, who recruited me and guided me along the way. To the summer interns Andrew Mahon and Joshua Sullivan, I could not have conducted so many experiments in such a short amount of time or been able to get a working fixture so early in the project. None of this would have been as fun without my Combat Systems Applied Physics cohort, especially the guys in the MEMS office, Edd Wulff and Jamison Fiebrandt. Most of all, I would like to thank my beautiful wife, Genna, for her love and support during the many long hours and countless weekends all while she was at home looking after our beautiful daughter, Ava.

THIS PAGE INTENTIONALLY LEFT BLANK

## I. INTRODUCTION

Electric propulsion has been an attractive alternative to chemical rockets for deep space exploration and satellite station keeping for some time now. This is due in part to their high specific impulse and thus relatively low propellant mass utilization compared to conventional chemical rockets. Recently, a small but growing need for microsatellite and nanosatellite propulsion has taken shape due to the ever-increasing number of microsatellites (10–100kg wet mass) and nano-satellites (1–10kg wet mass) in Low Earth Orbit (LEO). This new *micropropulsion* industry comprises any form of electric propulsion that can fit in the CubeSat form factor and has thrusts in the mN range [1]. In particular, ion thrusters are of particular interest in this industry because compared to other electric propulsion schemes, large permanent magnets are unnecessary in their operation and inert compressed gasses can be used as the propellant. A high specific impulse is a major advantage over conventional chemical propulsion that requires a large storage space for the propellant and make up a significant fraction of the total vehicle mass.

A CubeSat is any nano-satellite that fits the form factor standard of  $1kg / U$ , where  $1U = 10cm \times 10cm \times 10cm$ . Typically CubeSats will be deployed from a rocket with a much larger and more expensive mission package or can be deployed directly from the International Space Station (ISS). However, for orbits below the ISS, CubeSats will be deployed by a spring mechanism at a predetermined time as the launch vehicle is heading to its primary mission. That being said, the U.S. Air Force, NASA and the National Reconnaissance Office (NRO) are reluctant to launch CubeSat missions that contain propulsion systems with compressed, toxic, or flammable propellants even if the propellant itself is inert. This is due to the possibility that a ride-along mission could cause catastrophic damage to the launch vehicle or the much more expensive primary payload. The Naval Postgraduate School (NPS) designed a CubeSat launching device that was flight tested as a secondary payload on NROL-36 on September 14, 2012 [2]. Figure 1 shows the NPS CubeSat launcher on the NROL-36 mission.

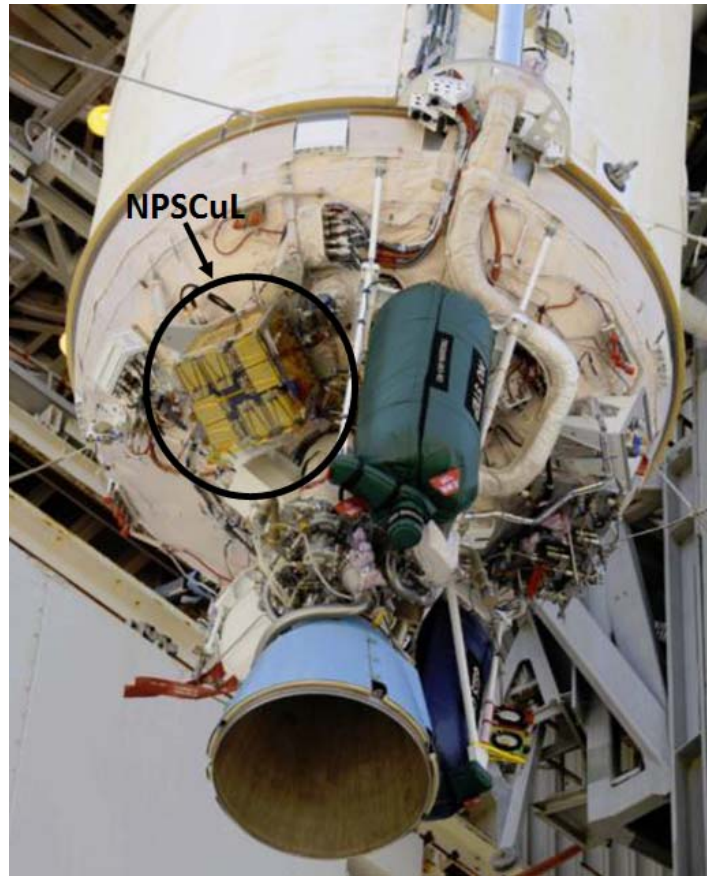


Figure 1. OUTSat mated to centaur stage of the NROL-36 mission.  
Adapted from [2].

CubeSat missions are providing the communications, intelligence, and scientific communities an increasingly viable LEO and Very Low Earth Orbit (VLEO) platform at much lower cost. The VLEO altitude range (250km–500km) is becoming much more attractive to industry due to a reduced probability of space debris colliding with much larger and more expensive satellites, telescopes and even the International Space Station operating in LEO (~400km). However, operating in VLEO requires some form of station-keeping capability due to atmospheric drag forces that are active in LEO [3]. This station-keeping can be accomplished in a variety of ways, such as: micro chemical propulsion, cold gas thrusters, electrospray thrusters, and even micro-ion thrusters. However, in VLEO the thruster would have to be operating almost continuously which is why ion

thrusters that have very high  $I_{sp}$  compared to chemical propulsion are so attractive. A list of micro-propulsion examples currently in industry can be found in Table 1.

Table 1. List of CubeSat micro-propulsion currently in industry.  
Adapted from [4]–[10].

Company	Model	Ionization Scheme/ Thruster Type	Propellant	Isp (s)	Nominal Thrust	Power Consumption	Form Factor
Accion	Tile-V1	Electrospray	Ionic Liquid	1500	1.8mN	25W	1U
Busek	BGT-X5	Chem Propulsion	AF-M315E	220-225	500mN	20W	1U
Busek	BIT-3	RF/IT	Xenon or Iodine	2100	1.15mN	75W	1.6U
Busek	BmP-220	PPT	PTFE	536	Unk	7.5W	0.33U
Phase4	RFT	RF/IT	Xenon	400-500	5.2mN	100W	1U
Vacco	C-POD	Cold Gas	R-134a	40	25mN	5W	0.8U
FOTEC	IFM-350	FEFP/IT	Indium	2k-5k	350uN	35W	0.66U

The standard CubeSat dimension of 1U denotes 1 liter of volume or 10x10x10cm.

Presently, a major capability gap in the CubeSat industry is orbital maintenance of the satellite. When several CubeSats are launched into LEO they are initially within a few kilometers of each other. As the CubeSat's orbit starts to decay the lower altitude satellite will have a higher velocity than a higher altitude satellite. This will cause the satellites to separate from each other over time. Therefore, if a CubeSat has a thruster capable of a delta-V that could maintain equal altitudes, formation flying would be achievable at a very low cost. This thesis presents a new generation of ion thrusters that can ionize any propellant, thus allowing for a clean safe thruster to be launched in the manner discussed previously. Figure 2 shows the FEFP thruster currently in use with the European Space Agency.

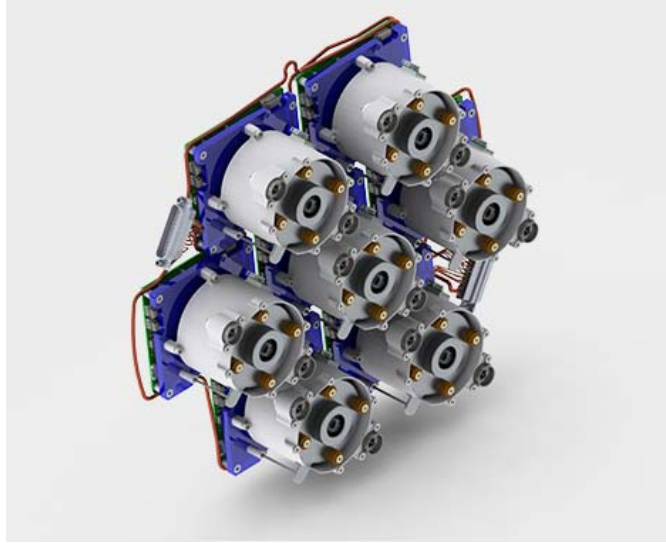


Figure 2. Cluster of ENPULSION IFM-350 FEEP thrusters. Source: [10].

## II. BACKGROUND

### A. PRINCIPLES OF ION THRUSTER ELECTRIC PROPULSION

Ion thrusters are a form of electric propulsion that can be described broadly in three fundamental categories, electrothermal, electrostatic, and electromagnetic. These three types broadly refer to the mechanisms by which a gaseous conductor is accelerated. Electrothermal thrusters heat the propellant electrically and expand the gas thermodynamically much like a chemical rocket. For electrostatic thrusters, “ion plasma acceleration is achieved by the interaction of electrostatic fields on non-neutral or charged propellant particles such as atomic ions” [1]. Electromagnetic thrusters, on the other hand, achieve ionic acceleration by the interaction of electric and magnetic fields within a plasma. The resultant electrostatic force density on either a charged particle or neutral plasma is described in [1] as

$$\tilde{\mathbf{F}} = \rho_e \mathbf{E} + \mathbf{j} \times \mathbf{B}, \quad (2.1)$$

where  $\mathbf{E}$  and  $\mathbf{B}$  are the electric and magnetic field vectors respectively,  $\mathbf{j}$  is the current density, and  $\rho_e$  is the charge density. For an electrostatic accelerator, the charge density consists of positive ions whereby an electromagnetic accelerator has a net neutral charge density. The first term in the equation is known as the Coulomb force and the second term is the Lorentz force. In an electrostatic ion thruster, the Coulomb force alone accelerates the ion plasma. Hybrid electromagnetic thrusters utilize the Hall effect to accelerate the plasma.

In an electrostatic ion thruster, plasma generation is achieved by a variety of techniques to ionize a large fraction of the propellant [11]. Biased grids are then utilized to electrostatically accelerate the ion plasma to high exhaust velocities [11]. The mass fraction that is ionized is usually described as a Mass Utilization Factor (MUF) and is described in [11] as

$$MUF = \frac{\dot{m}_i}{\dot{m}_p} = \frac{I_b \mu}{e \dot{m}_p} = \frac{I_b}{I_{ideal}}, \quad (2.2)$$

where  $\dot{m}_i$  is the ion mass flow rate,  $\dot{m}_p$  is the propellant mass flow rate,  $I_b$  is the ion beam current assuming all particles in the stream have exactly one electron removed,  $\mu$  is the atomic weight of the propellant, and  $e$  is the fundamental charge  $1.6022 \times 10^{-19} C$ .

For an individually charged particle, the thrust can be described using conservation of energy assuming unidirectional flow and the kinetic energy added to the ions is retained until it becomes exhaust (i.e., assuming no ion interactions):

$$\frac{1}{2} \mu (v_x - v_i)^2 = eV_b \Rightarrow v_x = \sqrt{\frac{2eV_b}{\mu} + v_i^2}, \quad (2.3)$$

where  $v_i$  is the initial unidirectional ion velocity,  $v_x$  is the total unidirectional ion velocity, and  $V_b$  is the potential difference applied across the accelerator grids, or beam voltage. Therefore, the maximum ideal thrust for an electrostatic ion thruster is described as the time rate of change of the ions momentum and can be rearranged using Equation 2.3 in the following manner [11]:

$$T = \frac{dm_p}{dt} v_{exhaust} = \dot{m}_i v_x = I_b \sqrt{\frac{2\mu V_b}{e} + \left(\frac{\mu v_i}{e}\right)^2}. \quad (2.4)$$

A thruster's specific impulse ( $I_{sp}$ ) is a measure of performance and is defined as the ratio of the thrust to the rate of propellant consumption:

$$I_{sp} = \frac{T}{\dot{m}_p g}, \quad (2.5)$$

where  $g$  is the acceleration due to Earth's gravity,  $9.807 m/s^2$  [11]. This is in effect a measurement of a thruster's *fuel* economy. Using the thrust from Equation 2.4 in terms of  $I_b$  and  $V_b$  defines the specific impulse for any ion thruster, "where thrust is due primarily to the ions" [11]. The specific impulse has the unusual units of seconds due to the equation being in terms of the exhaust velocity relative to  $g$  [11].

## 1. Ion Thruster Design

Ion thrusters can be broken up into three basic components: the ion generator, accelerator grids, and a means to neutralize the exhaust beam. An ion thruster's generator region can vary in the method of producing ions to be accelerated, but the basic geometry of the ion thruster will remain the same. Figure 3 shows this typical geometry with an electron bombardment ionizer (thermionic cathode) as an example [1].

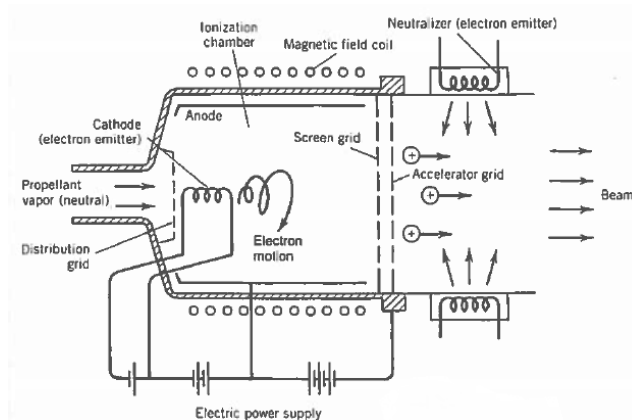


Figure 3. Simplified schematic diagram of an electron bombardment ion thruster. Source: [1].

In this configuration, the plasma generator consists of the cathode (electron emitter), anode, and magnetic field coils. As an inert gaseous propellant (usually Xenon or Argon) is forced to interact in the ionization chamber with the free electrons from the cathode, ions are formed. The magnetic field is introduced for electron confinement purposes, which increases the efficiency of the plasma generator. These ions are then accelerated through a series of grids and are then neutralized by a stream of electrons routed from the generator region. The resultant beam is a neutral plasma exhaust. The neutralizer is required because electrostatic charges would otherwise build up outside decreasing the thrust. External charge build-ups could also damage the internal electronics and interfere with communications arrays.

An ideal accelerator grid design consists of a three-grid system, the first grid collects residual electrons, the middle grid accelerates the ions and is at a high potential

(usually around 1,000V or more), and the final grid is used to keep the neutralizing electrons from entering the accelerator region [1]. Each grid hole is lined up in such a way that the ion beam can flow through uninterrupted [1] as seen in Figure 4. This configuration allows for ideal lensing to occur through the plasma sheath.

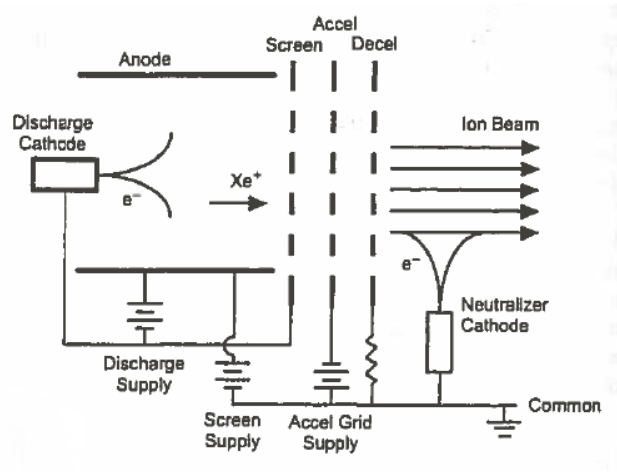


Figure 4. Simplified 1-D view of a three-grid accelerator system. Source: [11].

Beam current is more conveniently derived from the current density that is generated when plasma comes into contact with a metal electrode or *sheath*. This is the current per unit area that can pass through what is known as a planar sheath, and has a limitation due to space-charge effects [11]. The plane-parallel electrode accelerator configuration allows for a straight forward theoretical calculation of the maximum ideal thrust capability in an ion thruster assuming the initial velocity of the propellant particle is zero.

$$\frac{d^2V}{dx^2} = -\frac{\rho_e}{\epsilon_o} \quad (2.6)$$

$$j = \rho_e v_i = \frac{4\epsilon_o}{9} \sqrt{\frac{2e}{\mu}} \frac{(V_b)^{3/2}}{d^2} = 5.44 \times 10^{-8} \frac{(V_b)^{3/2}}{\mu^{1/2} d^2} \quad (2.7)$$

Equation (2.7) is the limiting or Child-Langmuir (CL) space charge current density, where the voltage in a one-dimensional space-charge region is found from Poisson's

equation (Equation 2.6),  $\epsilon_0$  is the permittivity of free space, and  $d$  is the distance between accelerator electrodes [1]. The ion beam current can be calculated in the following manner:

$$I_b = A_{PCB}j, \quad (2.8)$$

where  $A_{PCB}$  is the area of the PCB hole, and  $j$  is the current density. In equation 2.7, the current density is given in terms of the space charge density and the speed gained in the accelerator. The current density of a plane-parallel electrode is then found by solving equations 2.3 and 2.6 simultaneously. If the initial velocity of the particle to be ionized is non-zero, a correction factor must be applied to Equation 2.7 in the form [1], [12]

$$j_{\max} = j \left( \kappa^{1/2} + (1 + \kappa)^{1/2} \right)^3, \quad (2.9)$$

where  $\kappa$  is the ratio of the initial ion energy to the energy gained in the accelerator, assuming a monoenergetic ion plasma and is given by the following equation from [1]

$$\kappa = \frac{\frac{1}{2} \mu v_x^2}{e V_b}. \quad (2.10)$$

## 2. Ionization Methods

There are three main ionization schemes in ion thruster plasma generators, direct current (DC) electron discharges, radio frequency (rf), and microwave discharges. Each method presents its own challenges with complex power conditioning systems and the need for a large ionization chamber (Figure 3). For the overall ion thruster to be miniaturized, the ionizer and the ionization chamber need to effectively become one. This can greatly reduce the MUF, but the  $I_{sp}$  remains relatively high compared to cold gas thrusters. Table 1 shows a comparison of thrusters of varying ionization methods and size. This thesis explores a fourth ionization scheme that utilizes field ionization.

## B. FIELD EMISSION AND FIELD IONIZATION

This thesis continues the work started by Hicks in 2008 which investigated the use of a carbon nanotube (CNT) pillar array ionizer exploiting the field enhancement phenomenon to ionize Argon. Subsequent theses have continued that line of work creating test apparatuses for both field enhancement and later Field Ionization (FI). In [13], LT Hallan incorporated a thermal mass flow controller which allowed the experimenter to know the precise flow rate of Argon through the test sample. He also incorporated a micrometer in order to control the precise separation between electrode and test sample. In [14], LT Ozereko took the information learned from previous theses in the development of a test apparatus and showed a clear enhancement of the collected current with CNTs as opposed to the current collected from a sample without CNTs. To date, no NPS thesis has achieved FI in the laboratory in a way that the thrust could be verified and quantified.

### 1. Field Emission

In the case of field emission (FE), electrons are extracted from a metal by connecting it to an electric potential that is negative with respect to a local positive electrode. With no electric field applied, an electron in the metal must acquire a certain amount of energy to escape the metal's surface to become a free electron. The minimum energy for this to occur is known as the work function ( $\phi$ ) and is the difference of the minimum energy applied to obtain a free electron and the Fermi Energy ( $\phi = E_{\text{min}} - E_F$ ). The Fermi energy is the energy separating the valence band and the conduction band in a material and is a property of that material. The diagram on the left of Figure 5 shows the zero-field work function as well as the Fermi energy.

By subjecting the metal to a strong local electric field, the work function effectively reduces allowing a finite probability for an electron to tunnel through the barrier. The right image of Figure 5 shows the triangular potential barrier created by the localized electric field ( $V(x) = \phi - eFx$ ) where the first term is the work function and the second term is the applied potential.  $F$  is the applied electric field strength, and  $x$  is the

barrier thickness. The geometry of the metal should have a very fine edge so that an extremely localized electric field is formed at the tip.

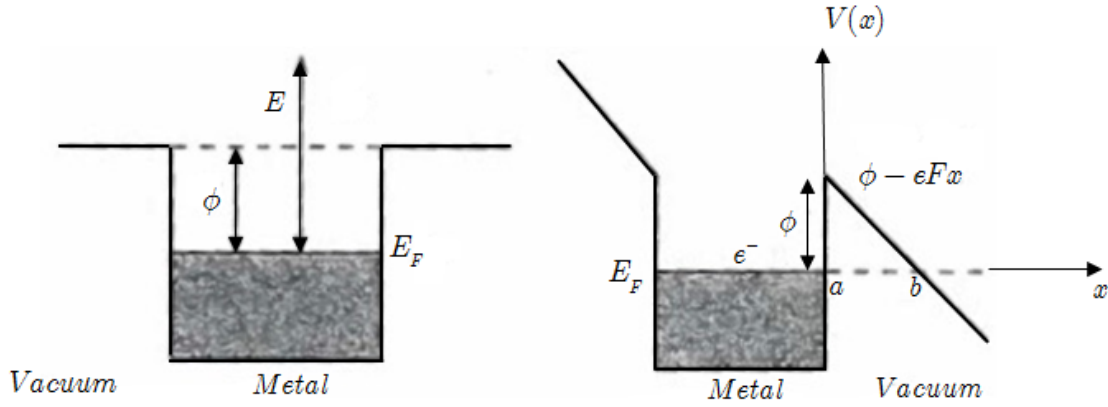


Figure 5. Field emission model potential well schematic.

The resulting electron current can be estimated by calculating the tunneling probability using what's known as the Wentzel-Kramers-Brillouin (WKB) approximation. Specifically, a potential barrier can be broken up into several thin barriers [ $q(x)dx \ll 1$ ] and the probabilities are integrated over the distance of the total barrier thickness:

$$P_T = \prod_i P_i \approx e^{-2\sum_i q(x_i)\Delta x} = e^{-2\int_a^b q(x)dx}, \quad (2.11)$$

$$q(x) = \sqrt{\frac{2m(V - E)}{\hbar^2}}, \quad (2.12)$$

where  $q(x)$  is the complex wave vector. For a known potential barrier and selecting the origin carefully (Figure 5), the probability of an electron to tunnel out of the metal is then

$$P_T = e^{-2\sqrt{\frac{2m}{\hbar^2}} \int_a^b \sqrt{(\phi - eFx)} dx} = e^{-F_0/F} \quad (2.13)$$

Because the current is proportional to the probability of a tunneling electron, the FE current can be estimated as

$$j = j_o e^{-F_o/F}. \quad (2.14)$$

Here, the current density proportionality constant ( $j_o$ ) must be analytically determined [15]. The resulting relationship is known as the Fowler-Nordheim (FN) current,

$$j = \frac{aE^2}{t^2(y)\phi} e^{\left(\frac{-b\phi^{3/2}}{E} \nu(y)\right)} \Rightarrow I \approx \frac{aS\beta V^2}{d^2\phi} e^{\left(\frac{-bd\phi^{3/2}}{\beta V}\right)}, \quad (2.15)$$

where  $E$  is the applied electric field,  $t(y)$  and  $\nu(y)$  are tabulated functions,  $S$  is the emitting surface area in  $\text{cm}^2$ ,  $I$  is the collected electron current,  $V$  is the applied electric potential,  $d$  is the electrode gap distance, and  $a$  and  $b$  are empirical constants known as the first and second FN constants respectively ( $a = 1.541 \times 10^{-6} \text{ A eV/V}$  and  $b = 6.831 \times 10^7 \text{ eV}^{-3/2} \text{ V/cm}$  derived for CNTs) [15]–[17]. With the application of CNTs, the local electric field needs to be converted into an enhanced electric field ( $E_{enh}$ ) due to the high electric field generated at the CNT tip:

$$E_{enh} = \beta E = \beta \frac{V}{d}, \quad (2.16)$$

where  $\beta$  is the field enhancement factor,  $V$  is the applied electric potential, and  $d$  is the distance between cathode and anode [16]. Substituting Equation 2.16 into 2.15 and taking the logarithm of both sides puts the relationship in the plottable linear form

$$\ln\left(\frac{j}{E^2}\right) = \left(\frac{-b\phi^{3/2}}{\beta}\right)\left(\frac{1}{E}\right) + \ln\left(\frac{aE^2}{\phi\beta^2}\right), \quad (2.17)$$

$$\ln\left(\frac{I}{V^2}\right) = \left(\frac{-bd\phi^{3/2}}{\beta}\right)\left(\frac{1}{V}\right) + \ln\left(\frac{Sa\beta^2}{d^2\phi}\right). \quad (2.18)$$

Here, the field enhancement factor can be found by experimentally extracting the slope of Equation 2.18 and solving for  $\beta$  as

$$\beta = \left( \frac{bd\phi^{\frac{3}{2}}}{m} \right). \quad (2.19)$$

Figure 6 shows what are known as FN plots from Equation 2.17. Figure 6 was generated from data collected at NPS by LT Chris Pace researching Free Electron Lasers [18]. Figure 7 is an example of FN plots for various samples [17].

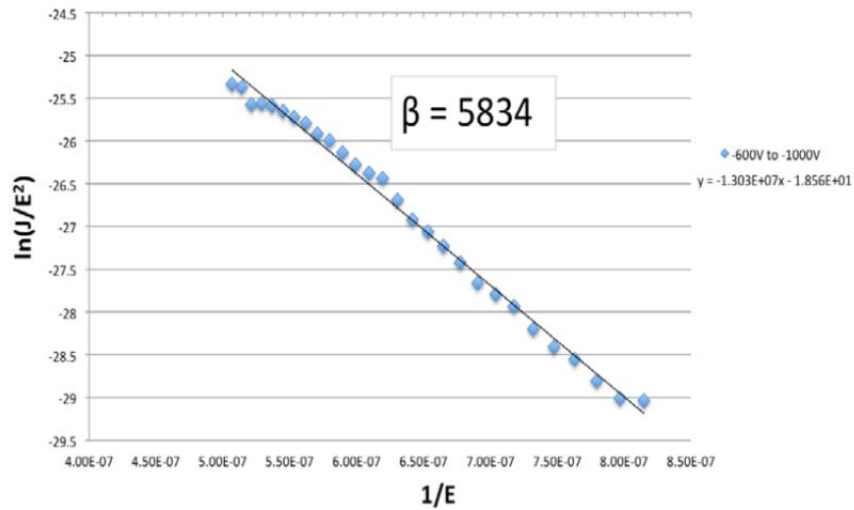


Figure 6. FN plot of an unpolished copper substrate with an electrode gap of  $500\mu\text{m}$ . Source: [18].

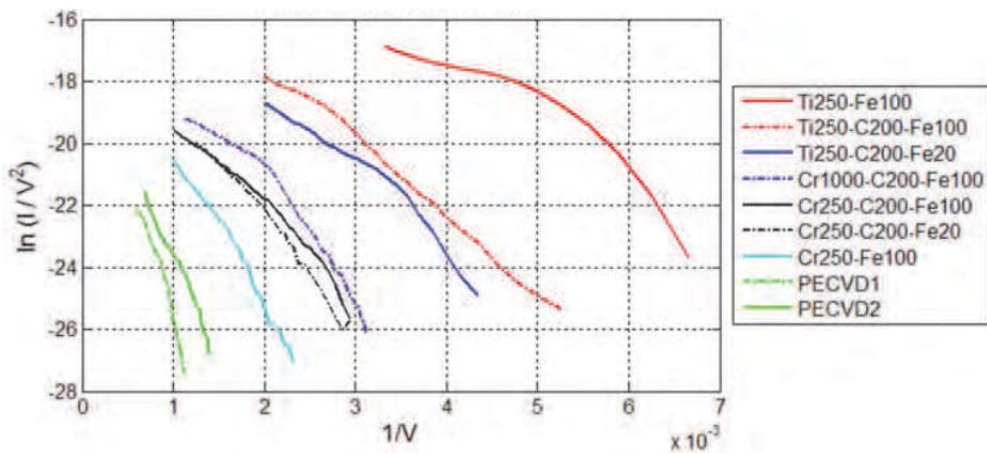


Figure 7. FN plot of selected samples. Source: [17].

## 2. Field Ionization

If the electric potential applied to the test sample electrode is positive, the mechanism reverses. In this configuration, the phenomenon known as Field Ionization occurs when a neutral gas comes into close proximity to the anode. Here, an electron is removed from an inert gaseous species and tunnels through a metallic surface via quantum mechanical tunneling in high electrical fields (usually between  $10^7 - 10^8$  V/cm). For FI to occur, the Coulombic barrier must be distorted by a high local electric field allowing for a finite probability of the electron to tunnel through the potential barrier. In Figure 8,  $B$  is the zero FI potential of the atom (also known as the electron binding energy of the atom),  $eFr$  is the applied potential energy, and  $V_I$  is the electron image potential. In the figure, the origin is established at the metal and the potential well is a distance  $r$  centered on a valence electron. The following FI theoretical quantum mechanical analysis assumes that the electrode through which an electron will tunnel is a featureless conductive metal. This thesis will expand this theory to FI through a CNT tip.

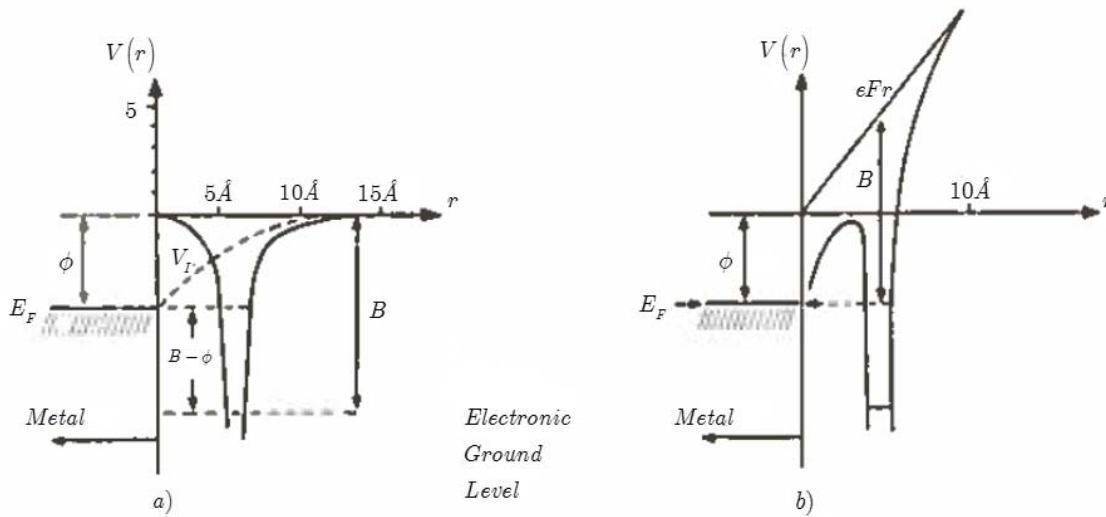


Figure 8. Field ionization model potential well schematic showing the Coulombic barrier (a) and the distorted potential well by the application of an electrical potential (b). Source: [19].

In this thesis, different experimental thrusters achieve FI through an array of angled-wall etched nozzles with a deposition of CNTs subject to a positive electric potential (the geometry of this electrode is discussed in future sections). As the inert gas atom approaches the CNT tip, a valence electron is removed from the atom and an ion is formed. The polarizability of the atom is directly related to the ease of ionization.

Equation 2.20 is the semi-classical analytic model FI potential adapted from [19],

$$V(r) = -\frac{Ze^2}{4\pi\epsilon_o(l_z - r)} + eFr - \frac{e^2}{4r} + \frac{Ze^2}{4\pi\epsilon_o(l_z + r)}. \quad (2.20)$$

The first term is the Coulombic barrier potential where the electrostatic interaction between charged particles is defined as:  $q_1 = Ze$  (Atom),  $q_2 = e$  (electron) where  $Z$  is the atomic number of the atom. The second term is the applied potential. The third term is the image potential of the electron and the fourth term is the “repulsion of the electron by the image of the ion in the electrode surface” [19]. Here,  $r$  is the distance of the atom to the electrode, and  $l_z$  is the atomic radius [19].

Because the valence electron in the atom may only tunnel to empty states at or above the Fermi level of the electrode, a critical distance must exist [20], [21]. If  $z_c$  is the critical distance (measured from the model potential electrode surface) and  $B$  is the binding energy of the electron in the atom, then the critical distance required for field ionization to occur can be found [20], [21],

$$eFz_c = B - \phi - \frac{e^2}{4z_c} + \frac{1}{2}(\alpha_a - \alpha_i)F^2. \quad (2.21)$$

Here, the third term is an image potential that takes into account the interaction of the newly created ion with the surface after tunneling has occurred [21]. The fourth term again, has the applied local electric field ( $F$ ) along with the polarizability of the incoming atom ( $\alpha_a$ ) as well as the polarizability of the newly formed ion ( $\alpha_i$ ) [21]. Neglecting the small image potential and the small polarizability term reduces the critical distance to

$$z_c = \frac{B - \phi}{eF}. \quad (2.22)$$

Using the model potential and assuming  $B$  is equal to the electron binding energy of the atom; the time-independent Schrödinger equation can be solved. As with FE, the WKB method can be used to determine the probability of tunneling, e.g. Equations 2.11-13, where the incident energy (total energy of the valence electron) in the case of FI is non-zero, and  $(E_I)$  is the first ionization potential of the atom in question (also known as the binding energy):

$$E_V = -eFl_z - eE_I + \frac{e^2}{4l_z}. \quad (2.23)$$

Therefore, by treating FI as a purely quantum mechanical event and knowing the probability that tunneling will occur, an expression for the frequency that an atom may come in contact with the potential barrier can be found [19]. Again, like FE, the origin must be taken carefully in order to evaluate the integral in Equations 2.11–13 (see Figure 8),

$$P_T = e^{-2\sqrt{\frac{2m}{\hbar^2}} \int_a^b \sqrt{(eV(r) - E_V)} dx}, \quad (2.24)$$

$$\tau = \frac{1}{P_T \nu} \simeq 10^{-16} e^{\left( \frac{0.68 E_I^{3/2}}{F} \right)}. \quad (2.25)$$

This equation has a very similar form to Equation 2.14 and is known as the lifetime [19]. However for FI, the current must be thought of in a different manner. Here,  $\nu$  is the frequency with which the valence electron in the atom strikes the potential barrier in a direction normal to it and has values ranging from  $10^{15}$  to  $10^{16} \text{ sec}^{-1}$  that are analytically determined (see [19]).

From this, the resultant current from FI is purely an ionic current and can be expressed as a function of particle flow rate ( $\dot{n}$ ) and the time it takes for an atom to pass through the critical ionization zone ( $t = dx/v(x)$ ).

$$I_{FI} = e\dot{n} \left( 1 - e^{-\frac{t}{\tau}} \right) \quad (2.26)$$

As the applied local electric field gets stronger, the lifetime term (Equation 2.25) gets smaller and the critical zone of ionization gets larger; Equation 2.26 becomes:

$$I_{FI} = e\dot{n} \left( 1 - e^{-\int_{x_a}^{x_b} \frac{dx}{v(x)\tau(x)}} \right), \quad (2.27)$$

which reduces to the classical FI current previously derived as the total ideal current possible in an ion thruster from Equation 2.2 since  $t \gg \tau$ .

$$I_{FI} = e\dot{n} = \frac{e\dot{m}}{\mu} = I_{ideal} \quad (2.28)$$

### C. CARBON NANOTUBE ELECTRODES FOR FIELD IONIZATION

Whether the goal is FI or FE, the electrode must be carefully designed so that the electrostatic geometry is optimal. This geometry is paramount to insure the best possible Mass Utilization Factor or Field Enhancement Factor can be achieved. Several previous and concurrent theses have worked to obtain the best possible angle for a nozzle that can still have an effective surface area for CNT deposition on a Silicon wafer [14], [22], [23]. Another idea is to use additive manufacturing to generate a micro pillar array nozzle. This thesis will only try to characterize the FI electrodes and therefore only briefly discuss the aforementioned manufacturing processes.

## 1. Angled-Wall Etched CNTs

Field ionization electrode samples were provided for characterization via ENS Alfred Garvey's thesis [23]. The samples provided were manufactured in the NPS Microelectromechanical Systems (MEMS) clean room and were an improvement on previous work [22]. ENS Garvey set out to manufacture an array of angled-wall etched nozzles on a cleaved  $1\text{cm} \times 1\text{cm}$  silicon chip, develop a recipe and a mathematical formula to determine the optimal angle of the side wall, as well as generate a theoretical formula for the MUF. He was successful in all three with the caveat that the etch into the silicon did not completely punch through the substrate. Hence, further etching from the underside of the sample was necessary to complete the nozzle (Figure 9).

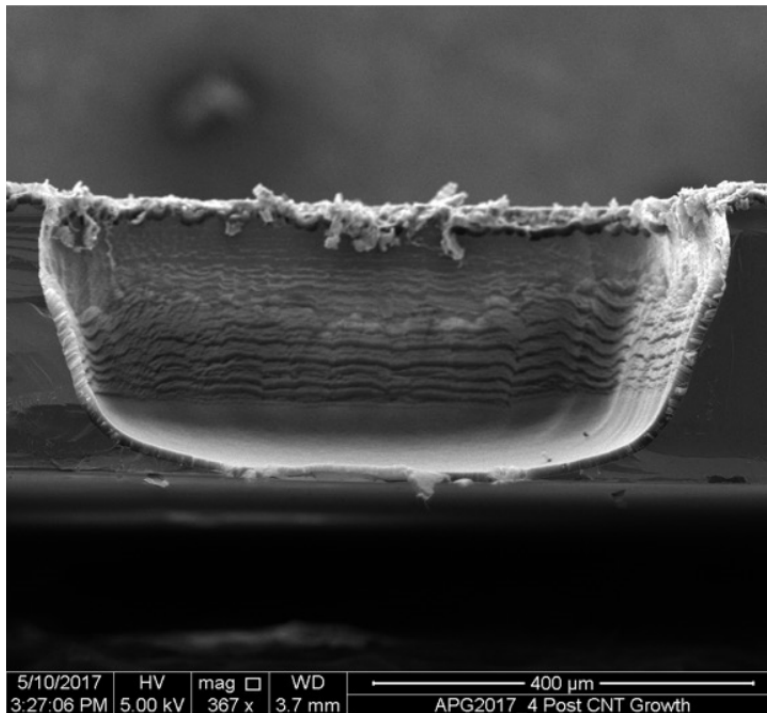


Figure 9. SEM micrograph: Nozzle cross-section after CNT growth.  
Source: [23].

The Nozzles provided from ENS Garvey's thesis had a calculated ideal MUF of 0.3% at a sidewall angle of 33 degrees [23]. The actual MUF from these electrodes will be determined in this thesis and then compared to the calculated ideal MUF.

## 2. Nano-Scribed Micro-Pillar Array Nozzle

Another Field Ionization electrode was manufactured at the Oak Ridge National Laboratory (ORNL) however will not be characterized in this thesis. This new electrode was manufactured using a nano-scribed manufacturing technique to generate a similar geometry to the angled-wall etched electrode, but micro pillars were added to greatly increase the possible ionization area within the nozzle. Figure 10 shows a Scanning Electron Microscope (SEM) micrograph of the Nano-scribed micro-pillar array nozzle.

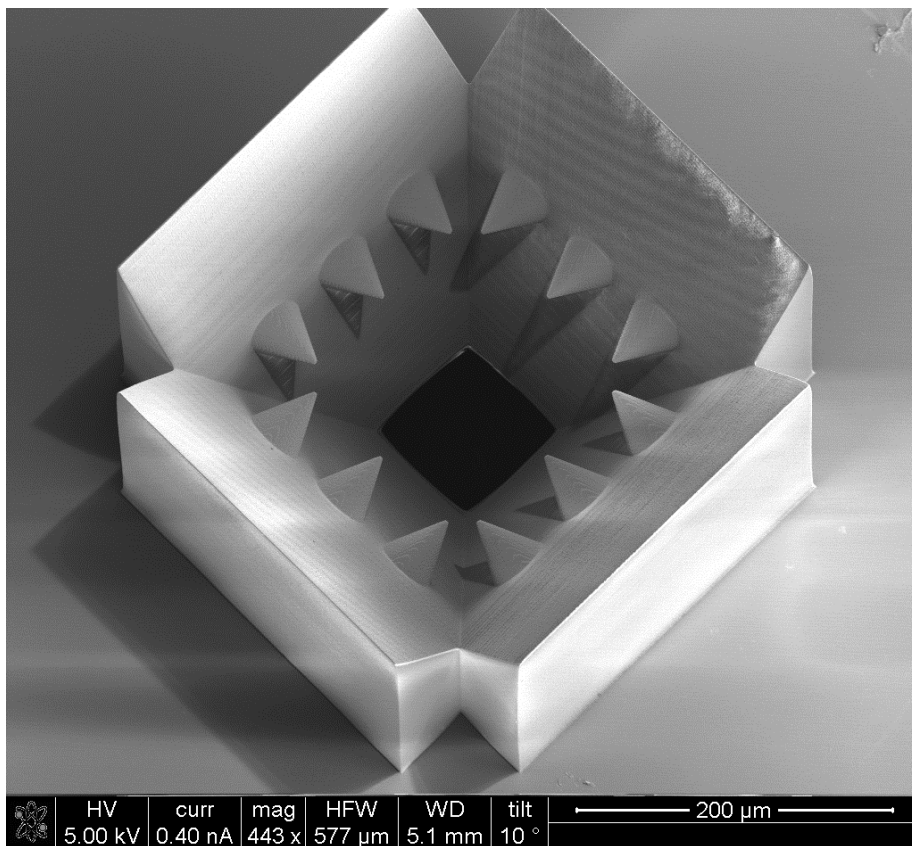


Figure 10. SEM micrograph of the nano-scribed micro-pillar array nozzle from ORNL.

## D. FIELD IONIZATION TEST CHAMBER

Characterization and thus experimentation of the manufactured samples is arguably the most important aspect of the Field Ionization Electric Propulsion (FIEP)

project at NPS. Each test apparatus has made significant progress in the pursuit of characterizing an FI electrode; however, they have yet to be able to characterize an electrode in a fixture that has the actual geometry of an ion thruster; or have they been able to achieve FI in the laboratory. A new FI apparatus sets out to do just that.

### **1. Limitations of Previous Test Chamber Generations**

Previous generations of testing apparatus could characterize CNT electrodes grown both at NASA Ames Research Center and at NPS. However, the first two generations of test chambers were unable to make finite changes to the separation between sample electrode and collector. Nor could they precisely control the flow rate of the test gas [24]. The third generation designed a completely new ionization chamber and incorporated a micrometer to control the electrode gap, and a thermal mass flow controller to know the exact mass flow rate of the test gas [13]. This was a major leap forward in the ability to characterize the electrodes being manufactured in the NPS clean room. However, the experiments conducted were only of FE and thus a field enhancement could only be shown by comparing blank samples to samples with deposited CNTs.

All previous generations could measure the beam current generated by the ionized gas, but due to the design of the ionization chambers, the researchers were unable to identify ion plasma visibly. There was also concern that the ionization was uncontrolled and the test sample may have been arcing to the walls of the chamber and thus the measured current was indistinguishable from breakdown current. Due to this, FI was never attempted using these apparatuses.

### **2. Fourth-Generation Test Chamber Objectives**

The fourth-generation testing apparatus will move this project into its next phase by taking what has been learned about testing various electrodes and giving follow on research a platform to conduct both FE as well as FI experiments. As stated before, FI

was never observed using the previous equipment; therefore, this new apparatus will focus on building a platform to characterize FI electrodes.

The objectives of this thesis are to design an apparatus to test any concurrent FI electrode which must be modular and repeatable. A completely new kind of vacuum chamber is utilized in order to observe ion plasma generated from FI. It is the first at NPS to attempt to build a working ion thruster with measurable thrust and ion beam current. Argon is the primary propellant for this thruster which must be introduced to the thruster in a manner that does not jeopardize the vacuum. A mass flow controller is incorporated in the Argon injection system; however a micrometer to precisely control the electrode separation will not be utilized. Instead, a fixed separation distance of the sample electrode and Accelerator Mesh Grid (AMG) will be maintained.

THIS PAGE INTENTIONALLY LEFT BLANK

### III. EXPERIMENTAL APPARATUS

#### A. DESIGN OF THE FOURTH-GENERATION TEST CHAMBER

The fourth-generation test apparatus at NPS drastically changed the direction of the FI electric propulsion project at NPS by designing a first ever ion thruster test fixture. This fixture brought forth several engineering challenges that were not experienced on previous generations of apparatuses. The overall data acquisition suite and the means by which a test gas was to be presented to the test sample had to be completely redesigned. No exposed electronics were able to be in the bell jar assembly; this included, at least for now, the possibility of using a micrometer for precise gap control in the ion thruster. Figure 11 is a block diagram of the overall test chamber, the vacuum pump, the Argon injection system, and the data acquisition suite for measuring ion thruster beam current.

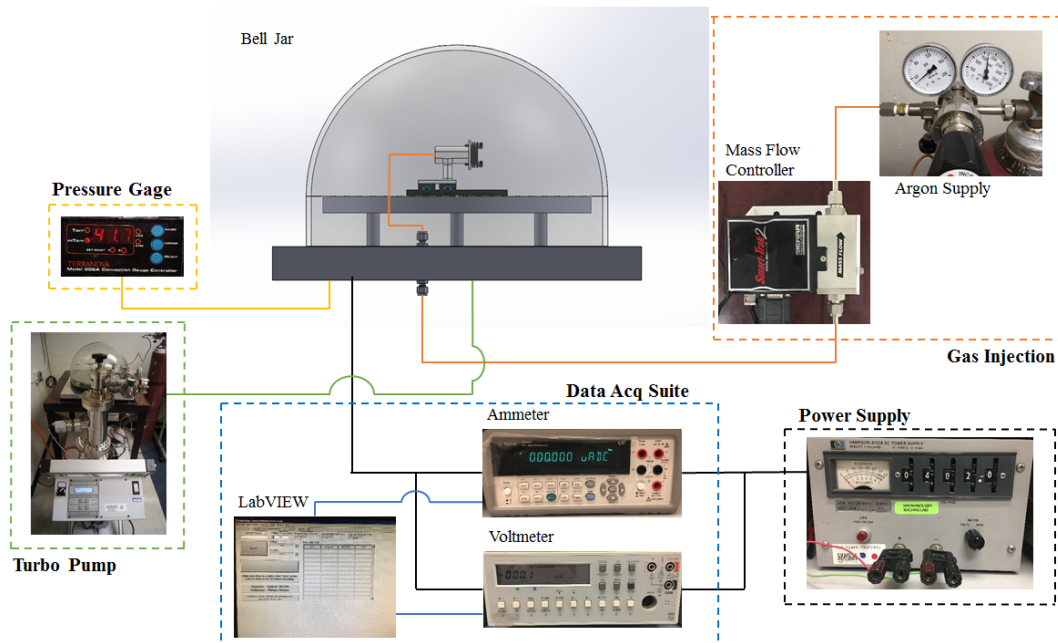


Figure 11. Block diagram of the FI test apparatus and the High Voltage–Current Measure DaQ suite.

## 1. Vacuum Chamber (Bell Jar) Construction

The vacuum chamber used in this thesis was of the bell jar and baseplate design class. It consisted of a Kurt J. Lesker Co. 18in OD Pyrex bell jar with a plastic L-shaped gasket. The baseplate was an Aluminum block with a 1/4" tube fitting gas injection port, six electrically insulated DE-9 male connectors, four electrically insulated DB-25 male connectors, five female BNC connectors, a 1/2" evacuation port, and a 1/8" NPT pressure gauge port. A vacuum is drawn using a Varian Turbo-V 301-AG turbo pump and can maintain a sub 10 mTorr vacuum with no Argon gas flow and 30–40 mTorr at an Argon mass flow rate of 2g/hr. Pressure is monitored using a Terranova Model 906A Convection Gauge Controller and a MKS/HPS Convection Enhanced Pirani Gauge Sensor Tube (model CEP-HPS-SH) with a shielded 1/8in NPT port directly attached to the baseplate. A steel plate with three peg legs (electrically isolated from the base plate using Teflon sheets) and an array of 1/4"-20 threaded holes was used to affix an optical rail for rapid experimentation as seen in Figure 12.

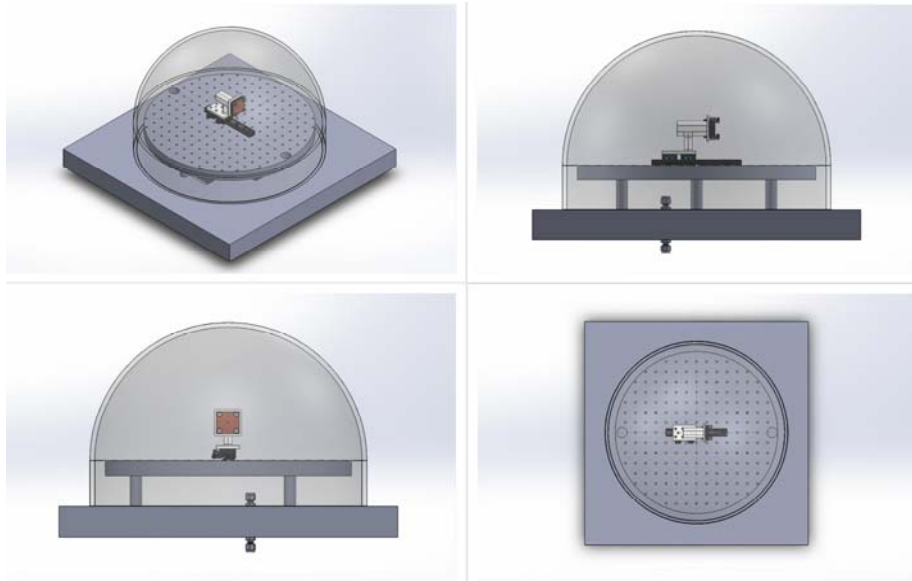


Figure 12. 3D CAD representation of the Bell Jar vacuum chamber and plasma generator apparatus.

## 2. Field Ionization Test Apparatus

The FIEP test apparatus can be broken up into several components: experimental fixture, thruster test assembly, mass flow controller, high voltage source, current measurement apparatus, and thrust stand. The following discusses each of these components.

### a. 3D Printed Experimental Fixture

The goal of the FI test apparatus was for a modular and repeatable design. To do this, a 3D printed fixture was fabricated out of ABS plastic on a Stratasys model uPrint SE printer. The fixture had a flange with four 4-40 tapped holes and a 5/16" hole through the body of the fixture. Another 0.1" hole on the flange was added so that the wire from the plasma generator PCB would be unobstructed. This configuration was to allow for rapid reconfiguring of the plasma generator PCB and Accelerator Mesh Grid PCB as well as replacement of a test sample for rapid experimentation. A 1/4"-18 NPT tube fitting was tapped right into the ABS material allowing for a continuous flow of Argon to be presented to the test sample. The base flange of the fixture allows for it to be mounted on an optical rail inside the bell jar. Figure 13 shows the 3D printed fixture as a CAD rendition.

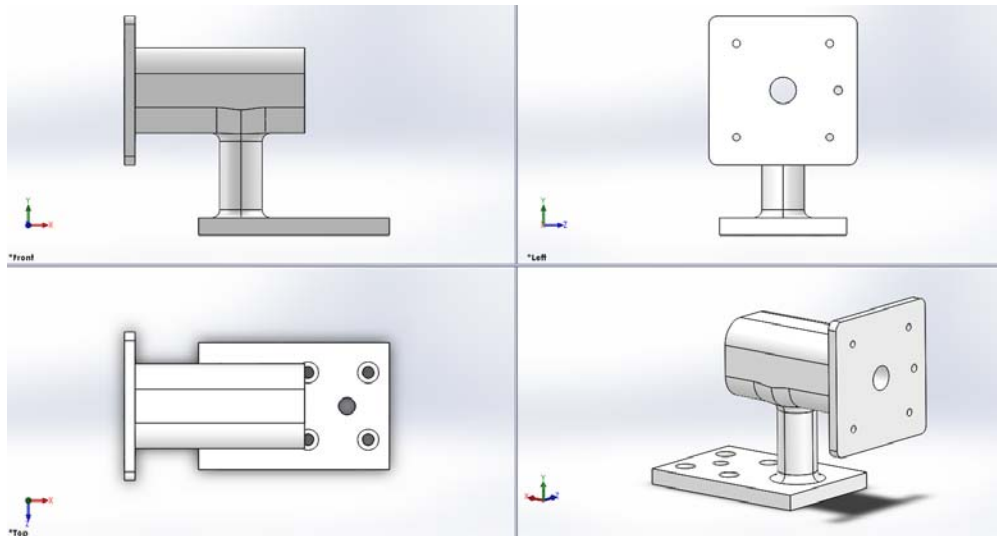


Figure 13. 3D CAD drawing of the FIEP experimental fixture.

***b. Complete Experimental Thruster Test Assembly***

In order to effectively electrically isolate and create an uninterrupted flow path for the ion plasma to be accelerated, a printed circuit board (PCB) was developed. The preliminary PCB design has a 0.2675” hole in the center and four 0.135” screw holes at each corner and was manufactured through an open source fabrication collective. The PCB substrate is made of several layers that consist of 1mil solder resist, 31.5mil 2oz Copper ground plane, 30mil FR4 core, and another 1mil solder resist.

The test sample and the Copper mesh are affixed to the electrodes via conductive Copper tape with the nozzle side of the test sample (the side with CNT growth) in contact with the ground plane. This is considered the nozzle configuration for the plasma generator. A wire is then soldered to a test point to create a potential difference between the AMG electrode and the FI electrode. The AMG was a 200 wires per inch Copper mesh with a 3mil opening. In order to ensure complete electrical isolation (i.e., no external subsequent ionizations outside of the ionization zone of the plasma generator) liquid electrical tape was liberally applied to the PCB test points. Figure 14 shows the plasma generator electrode with a sample loaded (anode) and the AMG electrode (cathode).

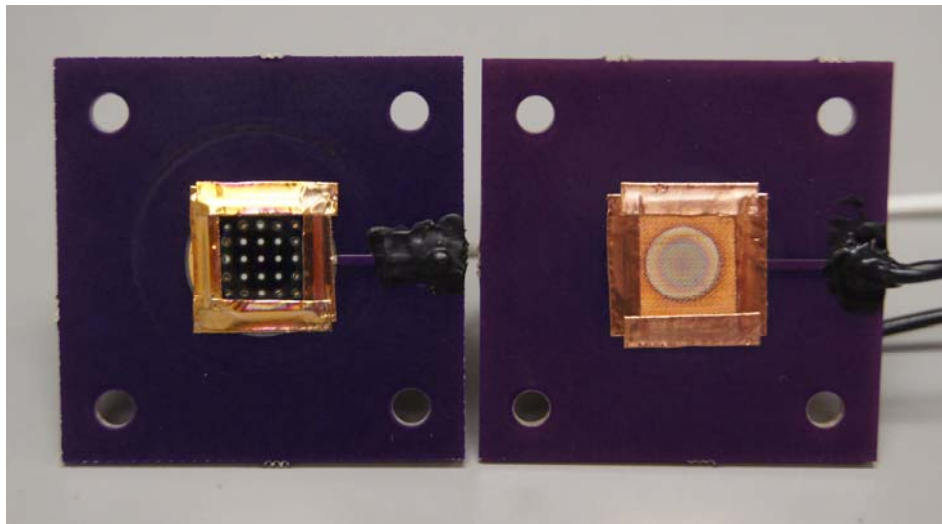


Figure 14. Plasma generator (left) and Accelerator Mesh Grid (right) PCBs post- experiment.

The entire ion thruster consists of the 3D printed fixture, the plasma generator PCB, the Accelerator Mesh Grid PCB, and finally a Copper plate with a small hole for ion plasma and unionized Argon to escape. Rubber O-rings were used as spacers between each component and plastic thumb screws secured the entire ion thruster to the 3D printed fixture. A fixed plasma generator and AMG configuration was opted for due to the bell jar configuration. Any caliper that could be used for precise gap control would have to be completely electrically insulated because electronics would have to be inside the bell jar under vacuum with an ion rich atmosphere. Figure 15 shows the complete FI test apparatus and Figure 16 shows the same but as an expanded view.

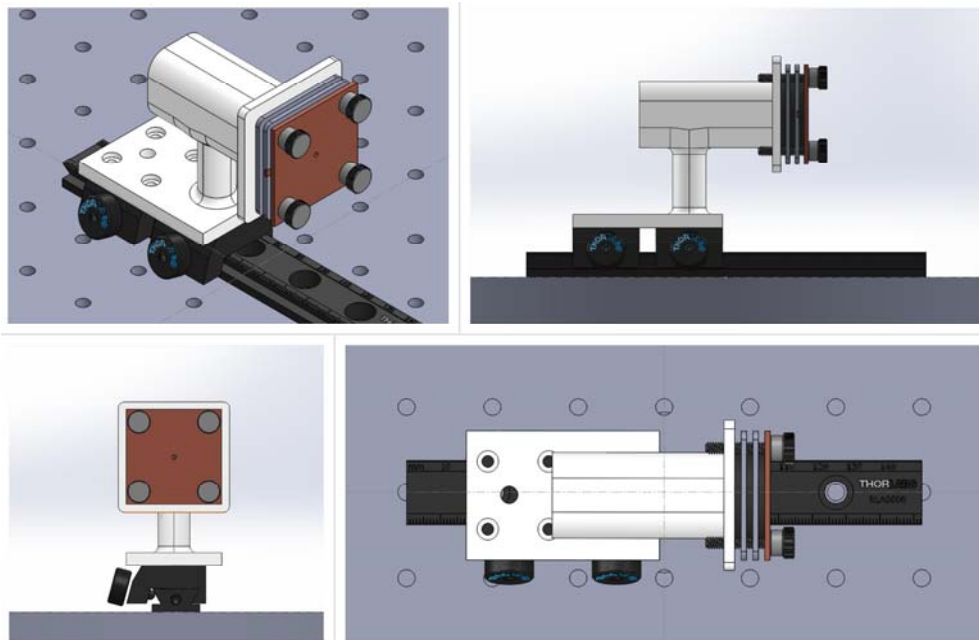


Figure 15. 3D CAD representation of the FI Test Fixture assembly.

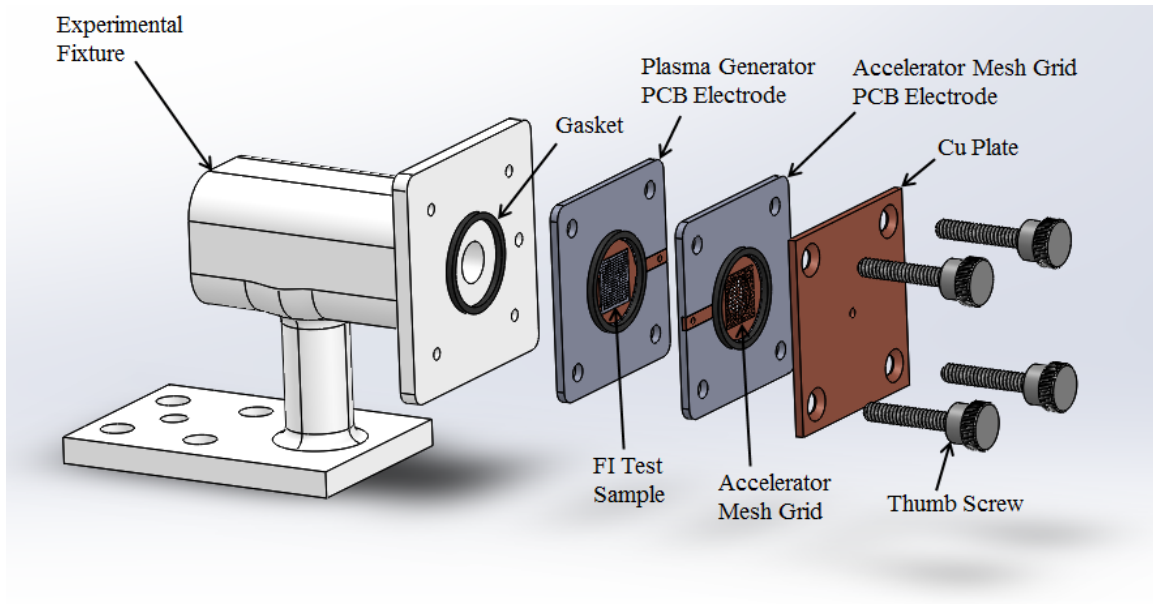


Figure 16. Expanded view of the FI Test Fixture assembly.

Power was applied to the plasma generator PCB via a wire directly soldered to the PCB test point. The wire was then run through a hole in the 3D printed fixture and connected to a BNC cable through the baseplate. The AMG and the Copper plate were connected to a common ground via a BNC cable through the baseplate. Both the FI electrode sample and the Copper mesh were affixed to the PCB ground plane by conductive Copper tape being sure to trim excess tape so that a good seal was made with the O-ring (see Figure 14).

### 3. Mass Flow Controller and Argon Gas Injection System

In order to provide the ionization gas at a known mass flow rate, a Sierra Instruments Smart-Trak 2 Series 100 Mass Flow Controller was utilized (Figure 17). This particular model has a flow range of 0–250scm (Dial-A-Gas) with an accuracy of  $\pm 1\%$  full scale [25]. Gas is drawn from a pressurized cylinder through a regulator and then supplied to the Smart-Trak 2. Gas flow enters the device through tube fittings and is separated into two paths. The main path is known as the Laminar Flow Bypass and the other is the Sensing tube as seen in the left image of Figure 18.



Figure 17. Sierra Instruments Smart-Trak 2 Series 100 Mass Flow Controller.  
Source: [25].

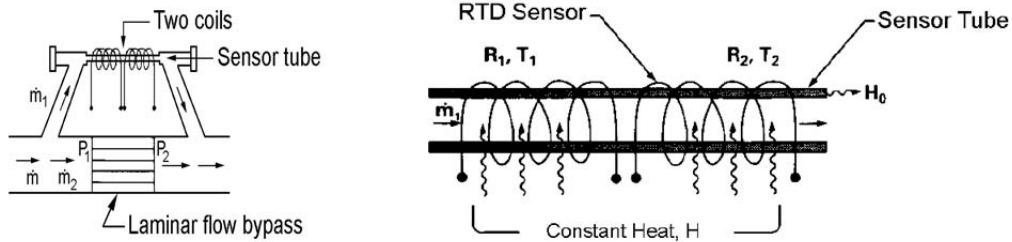


Figure 18. Flow paths through the Smart-Trak 2 Thermal Mass Flow Controller.  
Source: [25].

The operation of the Smart-Trak 2 is described in the Sierra Instruments instruction manual [25]. A small amount of gas is diverted through the sensing tube creating a pressure drop. The image on the right of Figure 18 shows two Resistance Temperature Detector (RTD) coils wrapped around the sensing tube. These RTDs direct heat ( $H$ ) at a constant rate into the gas stream, the heat is then carried from the upstream RTD to the downstream RTD. The microprocessor of the Smart-Trak 2 is then able to measure the resulting temperature difference ( $\Delta T$ ). From this measurement, Smart-Trak 2 calculates the output signal which is linearly proportional to gas mass flow. The final equation for mass flow from [25] is as follows:

$$\dot{m} = \frac{H - H_o}{C_p \Delta T}. \quad (3.1)$$

The thermal mass flow controller is then connected to the baseplate via tube fittings and PFA tubing. Inside the bell jar another PFA tube is connected via a PFA tube fitting that is directly plumbed to the 3D printed test fixture.

#### **4. High Voltage Source and Current Measurement Apparatus**

An HP Harrison 6110A High Voltage Power supply (rated for 0 – 3000V and 0 – 6mA) was used as the main voltage source for the plasma generator. The positive and negative (ground) terminals were connected to the baseplate via BNC connector. The positive lead is connected to the PCB containing the silicon wafer sample and the negative lead is connected to the copper collector plate. A wire attached to the same plate is soldered to the PCB containing the AMG. A second solid core wire is then connected to the collector plate and bent in such a way that the tip of the wire is approximately 1 cm away from the hole in the collector plate. This feature was added to collect the ion plasma escaping the plasma generator for measurement purposes as well as an additional ion accelerator mechanism.

Voltage being supplied to the plasma generator was monitored via a Phillips PM2525 Multimeter and connected in parallel directly to the test fixture. Current was measured via an Agilent 34410A  $6\frac{1}{2}$  Digit Multimeter across the positive lead of the plasma generator. Data from both Multimeters is then acquired using LabVIEW.

#### **5. Thrust Measurement Apparatus**

Thrust measurement was attempted using a Femto Tools model FT-S100/1000 cantilever force gauge (Figure 19). The force gauge was affixed to an optical experiment stand and the underside of the cantilever force gauge was presented to the ion plasma beam so that its circuitry was not directly affected by the ion plasma. Electrical tape was then wrapped around the apparatus to further isolate the circuitry. The force gauge was then connected to the baseplate via a DE-9 connector and then connected to a Femto Tools model FT-SC01 DaQ. Data was then collected via Femto Tools' proprietary software FT-WS01.



Image retrieved from <http://www.femtotools.com/products/previousproducts/ft-s-microforce-sensing-probe/>.

Figure 19. Femto Tools FT-S100/1000 cantilever force gauge.

## B. EXPERIMENTAL METHODS

Field ionization experiments were put into two categories, experimental thrust and beam current collection. The goal being to characterize a 1cm by 1cm cleaved sample manufactured at the NPS MEMS clean room by ENS Alfred Garvey [23]. Experiments were designed to determine if the electrostatic geometry of the sample allowed for a CNT deposited sample to outperform a sample with no deposited CNTs (blank sample). Collected Beam current would be the determining factor as to whether the CNT sample was in fact a better performing FI electrode. MUF,  $I_{sp}$ , and theoretical thrust would then be calculated from the collected beam current. Ultra-high purity Argon was used as the test gas to be ionized. In [14], LT Ozereko compared Argon to the industry standard propellant Xenon and determined that it is a suitable substitute for experimental purposes.

Beam current was collected by applying a positive DC voltage to the FI electrode starting at 490V and decreasing the voltage by 10V increments until no plasma was noticeable. This would typically occur at below 100 $\mu$ A. This threshold current is identical to the FE turn-on current in LT Ozereko's thesis [14]. Further discussion on what occurs once the 100 $\mu$ A threshold is reached can be found in the results section. After the turn-on voltage was determined, 500V would be applied and again the voltage would be increased 10V at a time up to 600V collecting beam current along the way. This process was conducted for three different mass flow rates on a CNT sample and a blank sample.

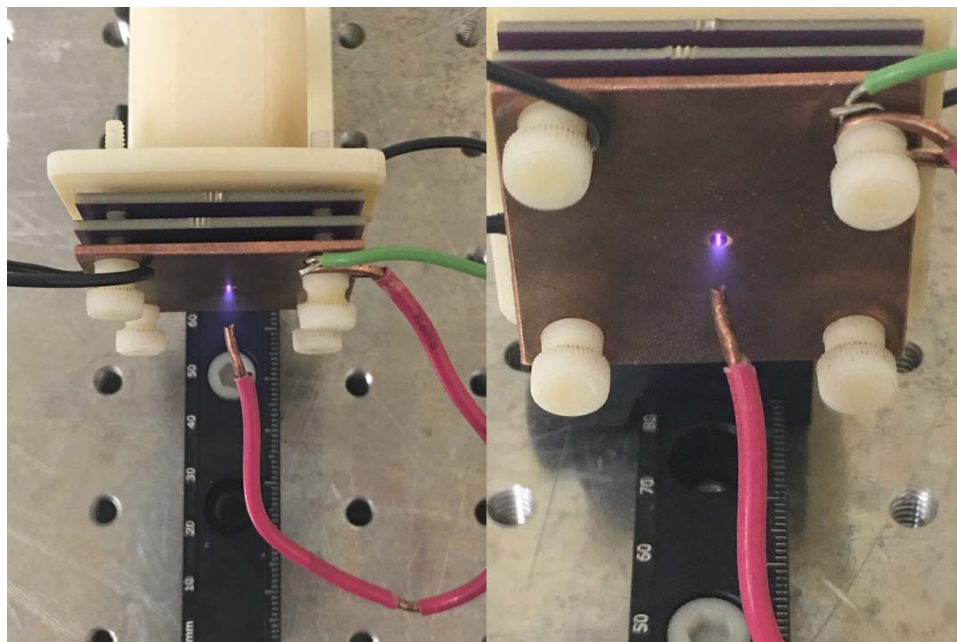
Great care was taken to document the amount of time each sample was subject to an electric field. Three experiments were conducted on a blank sample for a baseline and six experiments were conducted on a CNT sample from the same batch. Successive experiments were conducted on each sample in order to determine if there was any degradation to the CNTs or the wafer itself. PCBs were not interchanged for each subsequent experiment. The number of experiments that were able to be completed was directly related to the abrupt failure of a PCB. Therefore, the only difference between each experiment was the necessity to change out the AMG. This is because of the intense thermal effects on the Copper mesh.

Thrust measurement experiments were attempted by introducing a cantilever force gauge into the ion plasma exhaust. This was especially difficult due to the fact that the cantilever force gauge was a MEMS device that was placed in an ion rich atmosphere. If the gauge was not situated in the right position, ions from the plasma would crash the DaQ microcontroller. Experiments were conducted at a mass flow rate of 2g/hr so that interference with the MEMS device was minimized. Before any thrust measurements due to the plasma were collected, a measurement of full gas flow to no flow was recorded at 2g/hr, 2.5g/hr, and 3g/hr (see Appendix B). This experiment indicated that the gauge was working and it gave a baseline for future measurements. Before power was supplied to the plasma generator, full gas flow was applied to the cantilever force gauge and allowed to equilibrate. The data was then torn on the DaQ GUI enabling the data to have a zero point from which to read any resultant thrust once power was applied. Power was then applied starting at 400V and increased by 25V increments up to 600V. The power was cycled on for an amount of time where the thrust measurement reached a steady state and was then cycled off. This was repeated for several cycles at the same voltage to show a distinct turn-on and turn-off.

## IV. EXPERIMENTAL RESULTS

### A. FIELD IONIZATION RESULTS

The following discussion of the FI experimental results include a comparison of samples with CNT growth and samples with no CNT growth (Blank sample), the degradation of these samples, and a calculation of the MUF,  $I_{sp}$ , and theoretical thrust. For the CNT samples, two different samples from the same batch [23] were characterized varying the mass flow rate. The first CNT sample (known as CNT2) was heavily used during experimental development. The second CNT sample (labelled CNT3) was completely characterized from a fresh state to heavily used (six experiments total ~15.75 hours total exposure time). A single Blank sample (no CNTs deposited) was characterized in the same manner as the CNT sample and used as a baseline comparison (three experiments total ~5.5 hours total exposure time). Figure 20 shows visible ion plasma during a beam current collection experiment.



Argon has distinct purple ion plasma. The red wire was added to draw the plasma through the hole in an attempt to reduce leakage through the gaskets.

Figure 20. Ion plasma visible during a beam current measurement experiment.

Using a fresh Blank sample, and a fresh CNT sample the average current corresponding to a voltage was measured (top plot of Figure 21). Three experiments were completed for each and the data was concatenated into a single matrix. The average current value and the standard deviation across all experiments at the corresponding voltage were calculated. The error bars for each sample are the standard deviation across the three experiments. To keep all things equal, PCBs were not changed out for successive experiments. The bottom plot of Figure 21 shows a clear difference in a sample with and without CNTs deposited.

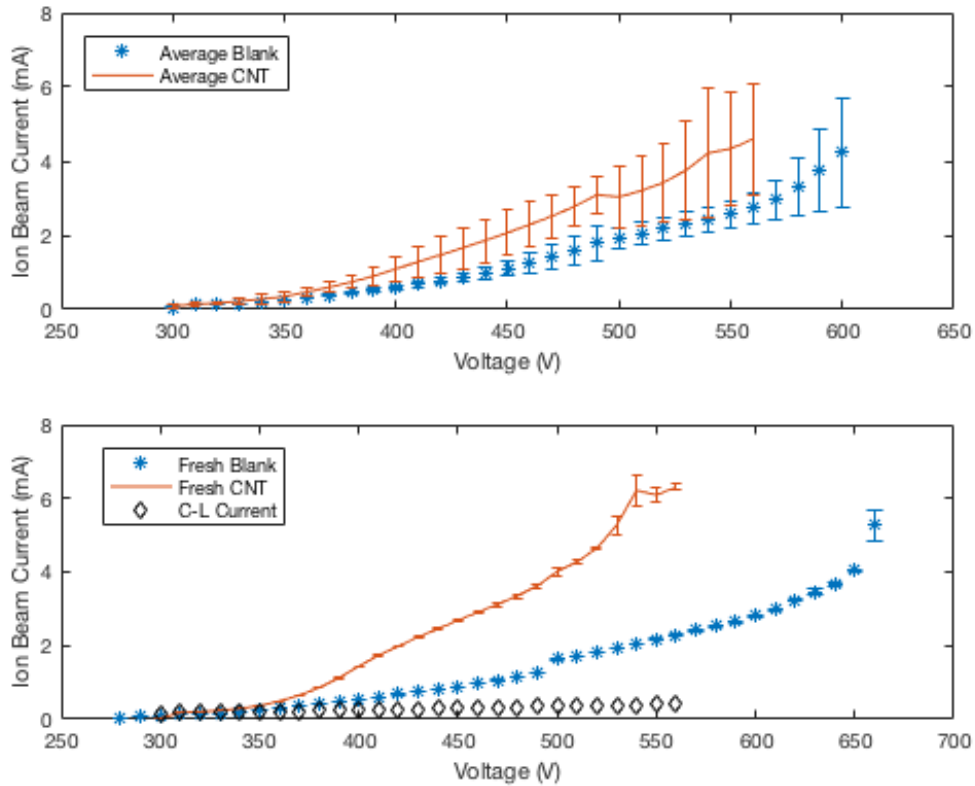


Figure 21. Top: average Blank compared to average CNT at 3g/hr, 3 runs each; bottom: fresh Blank compared to fresh CNT at 3g/hr as compared to theoretical CL current.

The fresh CNT and fresh Blank samples were also compared to the theoretical CL current from Equation (2.8). It appears that at low voltages and currents, the FIEP thruster follows the CL law. However, once the 100 $\mu$ A threshold is crossed ( $\sim$ 300V at 3g/hr), additional non-FI ionizations and currents become dominant (bottom plot of Figure 21). These additional ionizations are likely a result of the Townsend avalanche effect (Townsend discharge) transitioning to the glow discharge regime [26]. Townsend discharge is the phenomenon where free electrons are accelerated in a high electric field and collide with a gaseous species creating an ion and additional electrons [26], [27]. The result is an avalanche multiplication effect allowing electrical conduction through the gas. Equation 4.1 is known as the Townsend discharge current where  $I_o$  is the photoelectric current,  $\alpha$  is the first Townsend coefficient, and  $d$  is the distance between the cathode and anode.

$$I = I_o e^{\alpha d} \quad (4.1)$$

The first Townsend coefficient is defined as the number of secondary electrons produced by primary ionizing events per unit length and is given by the following equation [27]:

$$\alpha = PA e^{\left(\frac{B}{E/P}\right)}, \quad (4.2)$$

where  $A$  and  $B$  are experimentally determined constants,  $P$  is the gas pressure and  $E$  is the electric field between the cathode and anode. Figure 22 shows the current growing exponentially as it transitions to the glow discharge regime just before breakdown voltage.

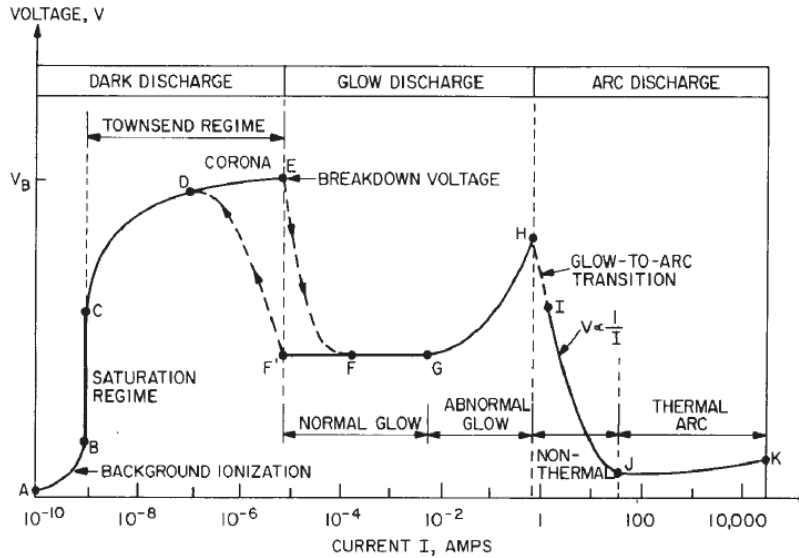


Image retrieved from [https://www.researchgate.net/figure/253328797\\_fig4\\_Figure-5-DC-Gas-Discharge-V-I-characteristics-10](https://www.researchgate.net/figure/253328797_fig4_Figure-5-DC-Gas-Discharge-V-I-characteristics-10).

Figure 22. Townsend avalanche regimes.

The voltage required to maintain an avalanche (known as the breakdown voltage) can be determined using the Paschen's curve where the voltage is plotted against the product of pressure and cathode/anode gap distance. Further explanation of this phenomena and simulation can be found in a concurrent thesis by LT Jamison Fiebrandt [28].

The following plot shows how the CNT sample degrades after each experiment (top plot of Figure 23). Each experiment was conducted using a fresh AMG and the first experiment was performed on a fresh PCB. Each successive experiment used the same PCB. Error bars were calculated from the standard deviation of the current measurement at the corresponding voltage. Run 6 replaced the PCBs of the plasma generator and the AMG to determine if PCB degradation played a role in the beam current degradation. The plot shows that we can draw a conclusion that the PCB does not significantly affect the degradation of the current. Instead, the PCB will fail abruptly (glow discharge to arc discharge, Figure 24). Therefore, the CNT sample alone degrades after each successive use. Curiously, the Blank sample beam current increased after each successive experiment (bottom plot of Figure 23). More runs on the same Blank sample were attempted but arcing (breakdown current) prohibited further experimentation.

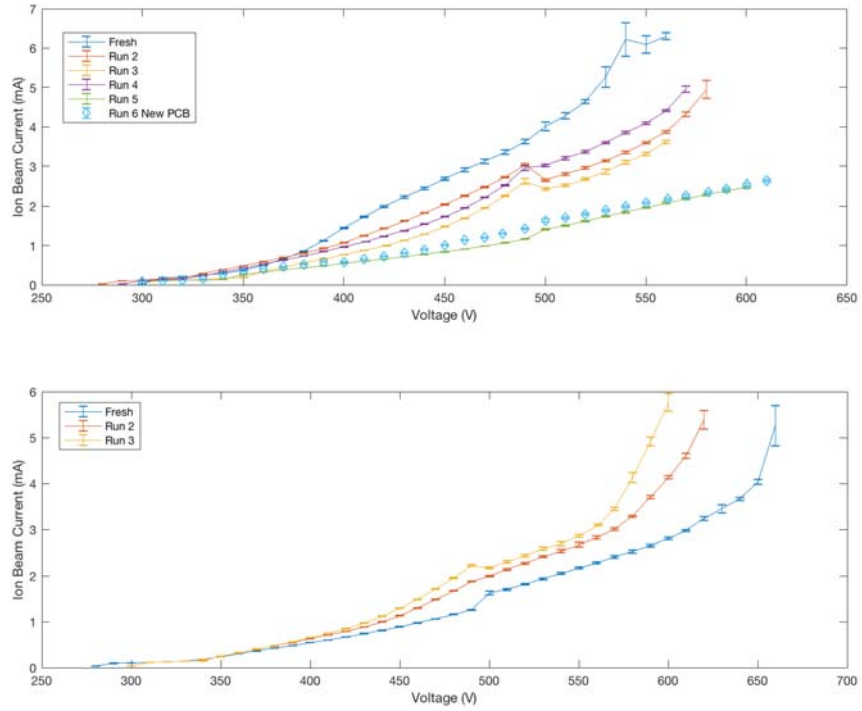


Figure 23. Top: Ion beam current versus voltage (multiple CNT runs at 3g/hr), bottom: Ion beam current versus voltage (multiple Blank runs at 3g/hr).

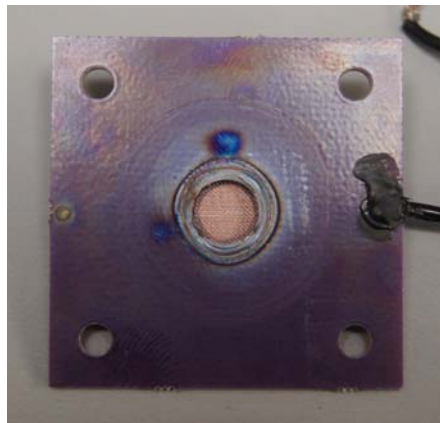


Figure 24. Arcing through the FR4 substrate causing a failed experiment.

Figure 25 & 26 Show SEM micrographs of an unused sample and a heavily used sample with and without CNT deposition. The heavily used CNT sample seems to have a layer that completely coats the CNTs ((B) of Figure 25). This could be the reason for a

decrease in collected beam current after each use (top plot of Figure 23). This can also be the explanation for the increase in collected beam current after each use of the Blank sample. The theory being that a deposited layer would create sharper edges and points on the Blank surface creating a field enhancement effect (bottom plot of Figure 23 and a noticeable difference between (A) and (B) in Figure 26).

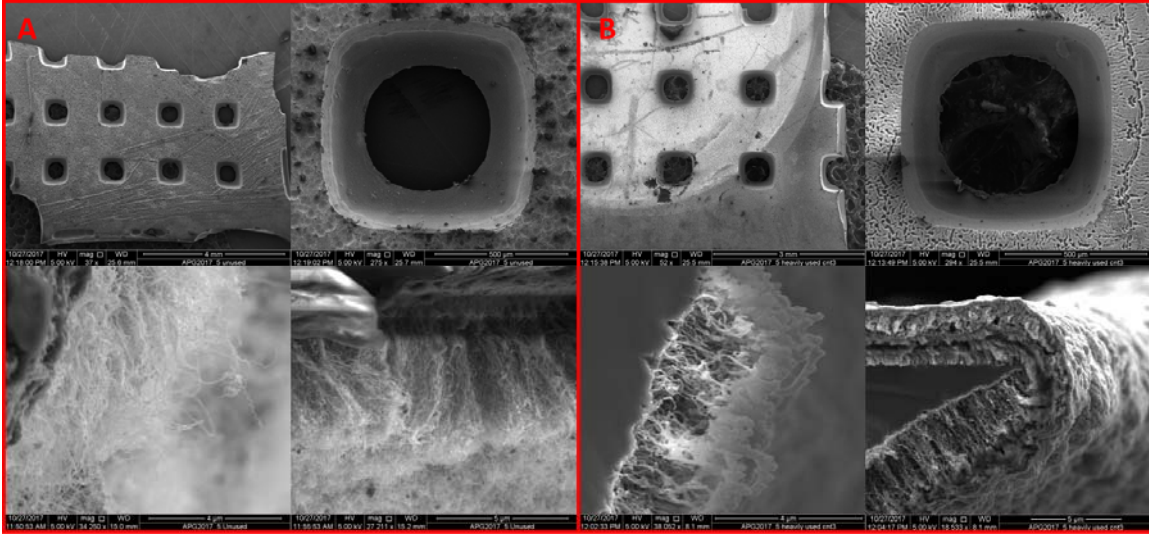


Figure 25. SEM micrographs of an unused (A) and heavily used (B) APG2017\_5 sample with CNT deposition.

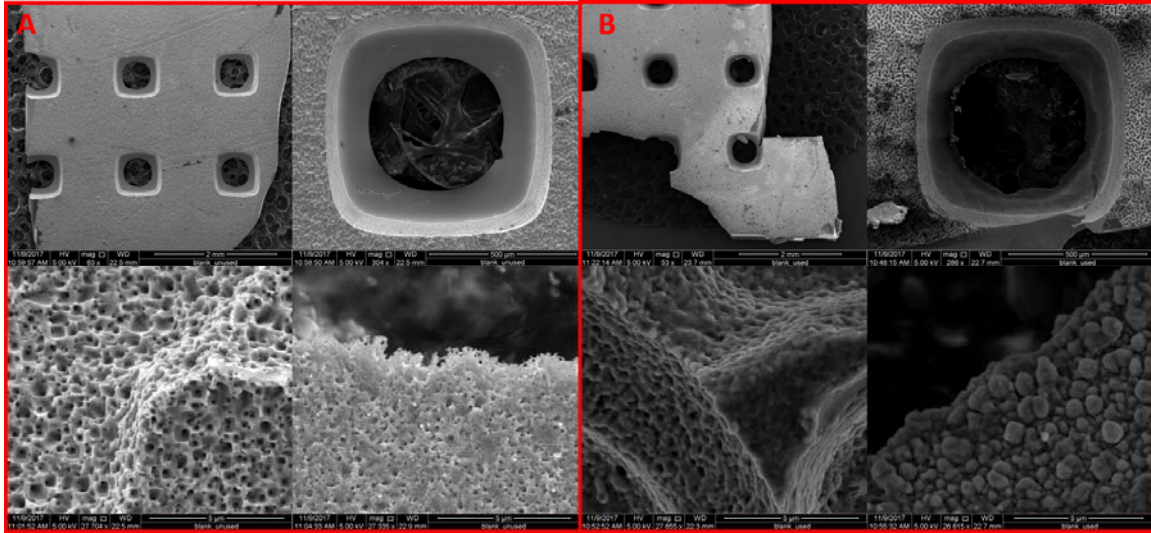


Figure 26. SEM micrographs of an unused (A) and heavily used (B) APG2017\_5 Blank sample.

Figure 27 compares the effects that a fresh sample (A) and a heavily used sample (B) have on the AMG. It appears that the fresh sample caused a larger burn area which coincides with a larger collected beam current for fresh samples. The comparison also shows a heavy buildup of a material on the fresh mesh. The right most image (C) shows a clean unused Copper mesh for comparison.

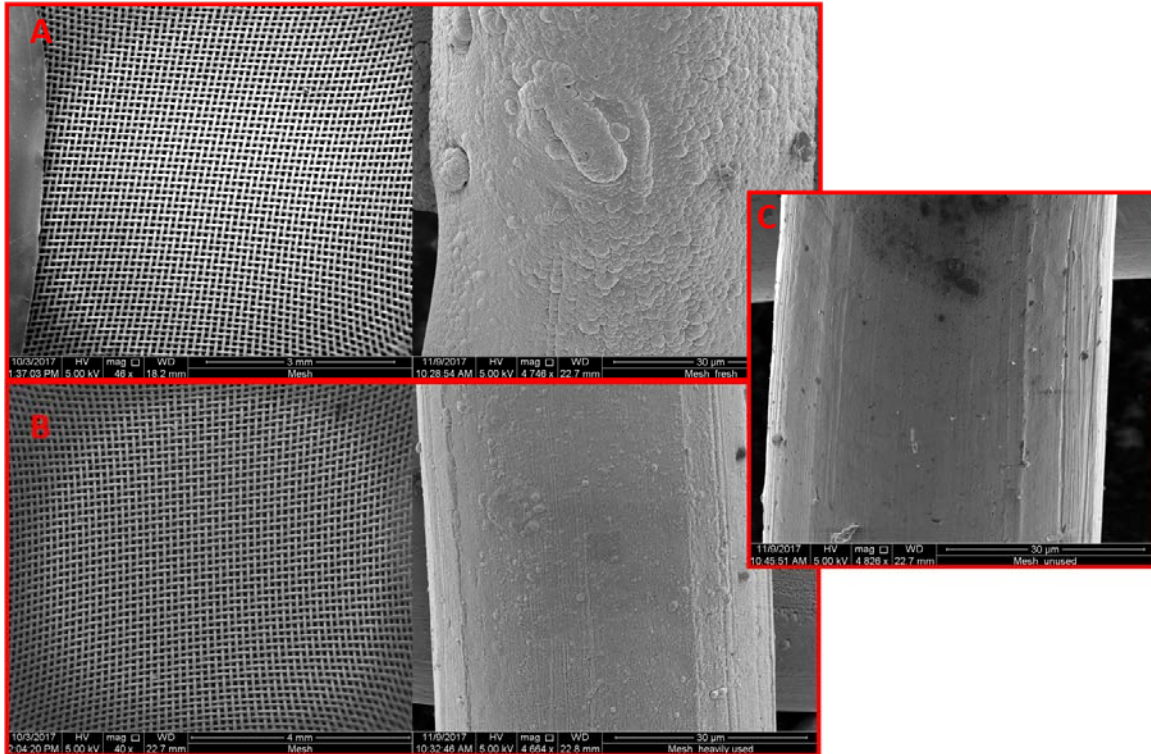


Figure 27. Comparison of SEM micrographs of the AMG condition after a Fresh sample (A) and a heavily used sample experiment (B), (C) is a micrograph of an unused Copper mesh.

Figure 28 depicts the calculated MUF,  $I_{sp}$ , theoretical Thrust, and power consumption from the collected beam current of CNT3 and the Blank sample. There is a distinct improvement in all three plots when the sample has CNT deposition. The  $I_{sp}$  of the experimental FIEP was well below the in-service thrusters shown in Table 1, which can be attributed to the low power consumption of the experimental apparatus ( $< 4W$ ). The low MUF can be attributed to geometry because the beam current collected is only representative of the captured ions in the AMG. The escaping accelerated ions are lost as exhaust.

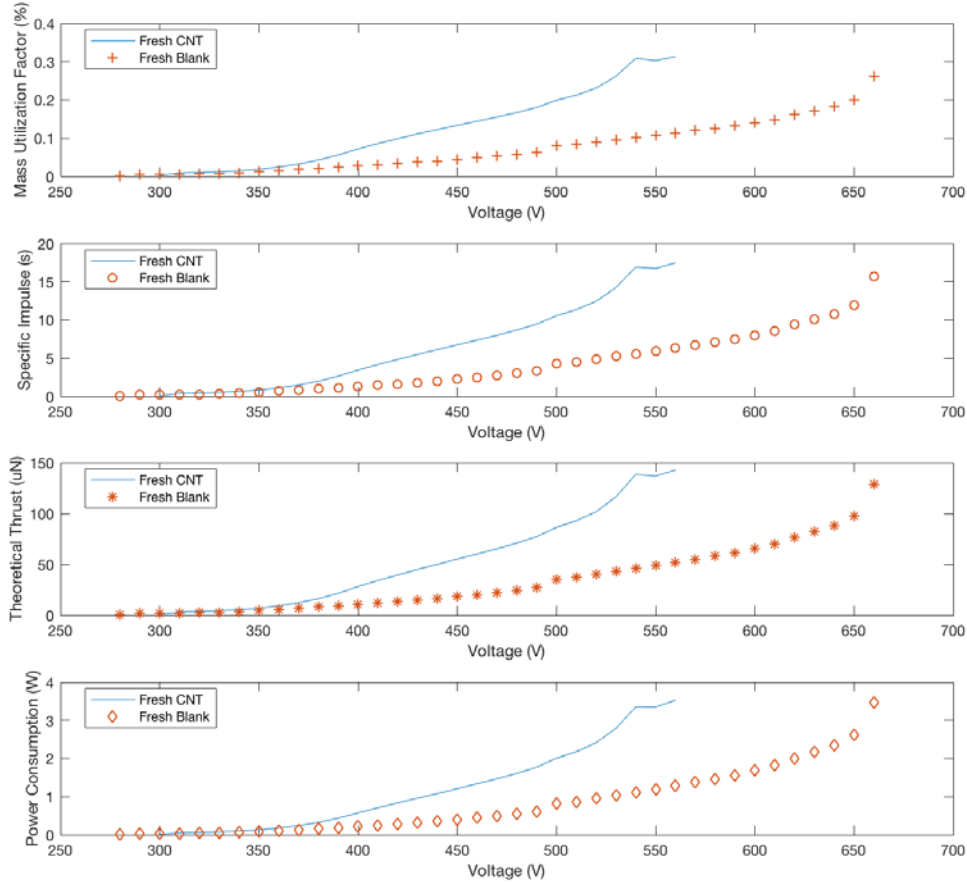


Figure 28. 1) MUF for fresh Blank compared to fresh CNT at 3g/hr, 2)  $I_{sp}$  for fresh Blank compared to fresh CNT at 3g/hr, 3) Calculated Thrust for fresh Blank compared to fresh CNT at 3g/hr, 4) FIEP Power consumption.

Figure 29 depicts a comparison of the MUF varying the mass flow rate of Argon. The plot clearly shows that the MUF decreases with a decreasing mass flow rate. An attempt was made to determine if the plasma generator was being choked by Argon flow by reducing the mass flow to 0.5g/hr. It was determined that this was not the case. Instead, this experiment showed that below the  $100\mu A$  turn-on threshold—as discussed previously—the beam current follows the Child – Langmuir law or is in the Townsend discharge regime (bottom plot of Figure 28). Once the  $100\mu A$  threshold is reached, Townsend avalanche occurs and an exponential growth of collected current is observed. It must be pointed out that the mass flow controller has an accuracy of 1% full scale

putting the lowest flow rate for this model at 0.948g/hr [25]. Thus, the 0.5g/hr mass flow is below the rated tolerance of the Smart Trak 2 mass flow controller.

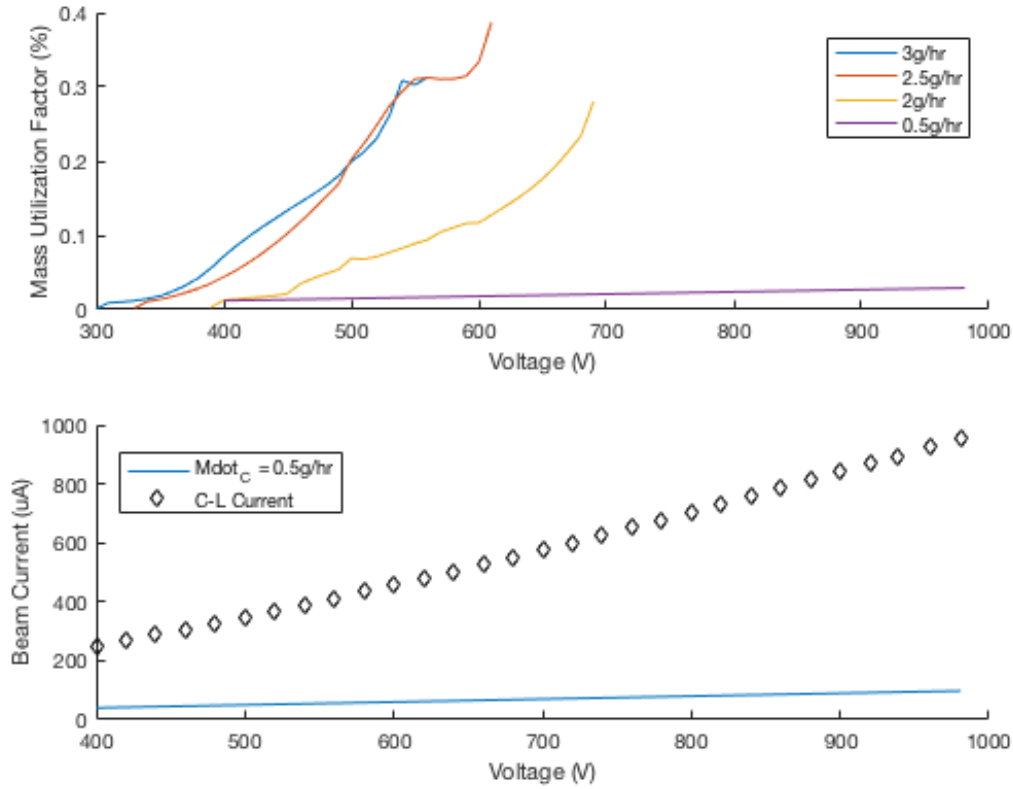


Figure 29. Top: Comparison of MUF to mass flow rate; bottom: beam current versus voltage at 0.5g/hr showing linear relationship below turn-on.

## B. EXPERIMENTAL THRUST

Thrust from the FIEP experimental thruster was measured using a thrust stand (FT-S1000 Gain: 496.6 $\mu$ N/V) placed directly in the plasma stream. Figure 29 shows the results of the thrust experiments compared to calculated theoretical thrust from the collected beam current of two different samples (Equation 2.4). The initial particle velocity  $v_i$  was calculated using the ideal gas law to find the density of particles and the continuity equation using the known mass flow rate. The figure also shows the  $I_{sp}$  calculated from the measured thrust. Only four voltages are displayed on the measured

thrust plot because 425V, 450V, & 475V were the only voltages that showed a positive trend. As the voltage increased, the force gauge became less reliable (as seen at 500V). The error bars are the calculated standard deviation across four experiments.

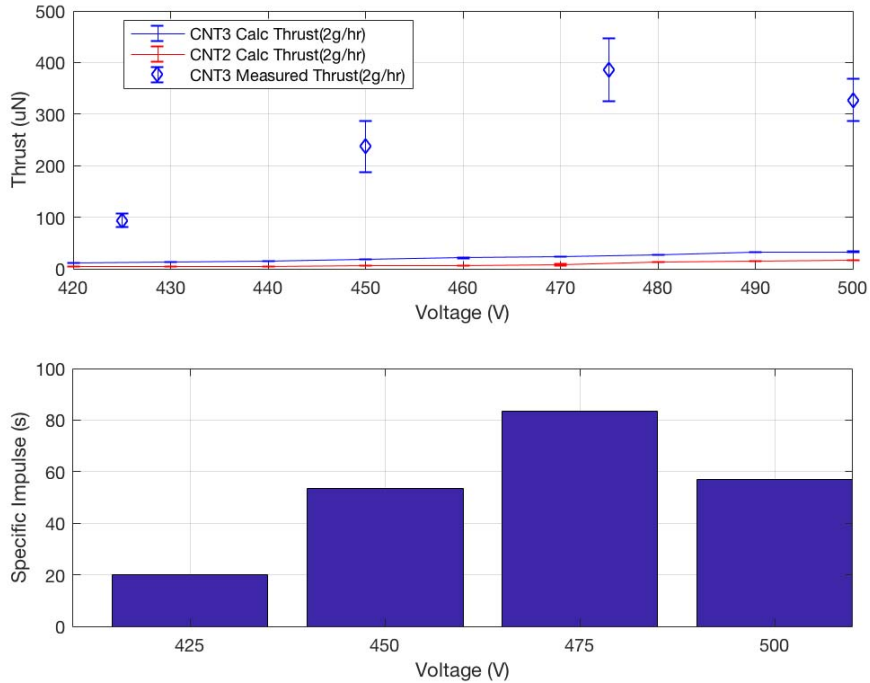


Figure 30. Top: comparison of measured and calculated thrust; bottom:  $I_{sp}$  from measured thrust (fresh CNT3).

Overall, the measured thrust in every case was significantly higher than the calculated thrust from measured current. It is thought that one of three things are taking place: 1) the ion rich atmosphere is affecting the MEMS cantilever force gauge giving an artificially high reading, 2) the beam current collected is only a fraction of the actual current produced by the thruster, or 3) the theory used in the theoretical thrust calculation is incomplete. In order to rule out the first train of thought, the thrust stand was rotated so that the cantilever was not in the plasma stream but the circuitry was in the same location as in its position during the actual experiments (see Appendix D). Measurements were then taken at the same voltages as before. The output was then averaged and subtracted

from the data in Figure 29. From this, it was clear that interference alone was not the sole reason for significantly higher results. All raw thrust data can be found in Appendix B.

## **V. CONCLUSION AND RECOMMENDATIONS**

### **A. SUMMARY AND CONCLUSIONS**

In this work, a fourth generation field ionization vacuum chamber and test apparatus was engineered and samples provided by a concurrent thesis were characterized as a proof of concept. The experimental method used on the samples was that of a baseline determination (Blank sample) compared to a sample with CNT deposition. The goal being to see if the deposition of CNTs actually provided an increase in collected current and therefore an increase in thrust. Measurements of FIEP thrust was attempted on the CNT samples using a MEMS device but was unsuccessful overall.

In conclusion, the test apparatus was capable of generating visible ion plasma and the data acquisition suite was capable of collecting beam current up to 6mA. The beam current collected showed a linear tendency up to 100 $\mu$ A and then a transition to exponential growth keeping the pressure and electrode gap distance constant while only varying applied voltage. From this observation, the exponential growth of current with voltage indicates the plasma is primarily formed by Townsend avalanche. The comparison of a CNT sample to a Blank sample proved that CNT deposition on an array of angled-wall etched nozzles increases the beam current. This can then be interpreted as a successful FIEP test apparatus proof of concept.

### **B. FUTURE WORK AND RECOMMENDATIONS**

As discussed previously, the vacuum chamber and FIEP test apparatus were an adequate proof of concept. The following is a discussion of the way forward in the pursuit of a prototype FIEP thruster and a fully capable FI electrode characterization suite.

#### **1. Field Ionization Test Apparatus**

Overall, the baseplate and bell jar vacuum chamber, turbo pump, mass flow controller, and power supply were sufficient for a series of proof of concept experiments. However, if this project is to move to a next phase, several items must be addressed.

***a. Power Supply and Circuit Design***

The power supply used for the FIEP was adequate for proof of concept characterization; however, an automated power supply (run by LabVIEW) with a sweep function and a high voltage current measure capability should be incorporated for future work. The previous power supply could provide up to 3000V but was unable to provide the necessary current required in this class of thruster. An excellent solution would be the Keithley High Power System SourceMeter™ (Model 2657A) which is capable of 3kV and up to 120mA.

The FIEP circuit should be updated with quick disconnects attached to BNC cables. During experimentation, the Voltmeter consistently showed a 2V difference from applied voltage. This could be due to an inefficient circuit design.

***b. Vacuum Chamber***

The current vacuum chamber pressure was insufficient (~5 mTorr no-flow) to simulate a space like environment at LEO ( $10^{-9} - 10^{-12}$  Torr). In order to characterize the FIEP thruster in a more realistic environment, a new vacuum chamber should be designed. Two options are a new base plate and bell jar, or a box chamber with a viewing port. The Kurt J. Lesker Company has a box chamber (Model: BX2424SACR) capable of high vacuum levels ( $10^{-5}$  Torr) with an acrylic door and configurable ports. This solution, however not at LEO pressures, would be a marked improvement to the current configuration. Another option is to add a second identical turbo pump in series to increase the pressure differential while using the same vacuum chamber.

***c. Mass Flow Controller***

The current mass flow controller is rated at 250scm full scale for Air with a 1% reported accuracy. Therefore, the lowest possible flow of Argon for the Smart-Trak 2 Series 100 is 0.948g/hr [25]. This is very close to the flow rates utilized in this thesis therefore it may be beneficial to incorporate a mass flow controller with a lower flow rate capability to reduce the uncertainty in mass flow. The Sierra Instruments Micro-Trak 101 would be a good solution.

## **2. Carbon Nanotube Electrodes**

The angled-wall etched CNT silicon wafer samples used in this thesis were grown on an un-doped silicon wafer. This makes the un-deposited side of the wafer (non-growth side) nonconductive. It is desirable to have the Silicon wafer be significantly doped so that the back of the wafer is conductive. This would be advantageous because the current configuration of the plasma generator is dictated by placing the Blank/CNT-growth side of the test wafer on the ground plane of the PCB to make an electrical connection. If the back side of the wafer were conductive, a more efficient electrical connection could be made and thus uncertainty in power transfer from electrode to Argon can be more certain. That being said, by supplying a known voltage and measuring the delivered voltage at the mounted sample with a Multimeter, the voltage drop is minimal.

From the results of the deterioration experiments, it became clear that for the angled-wall etched CNT electrode to be a viable FIEP electrode, fortification of the CNTs must be incorporated. What appears to be a heavy oxide layer buildup on the heavily used sample was clearly the culprit of a deteriorating beam current. If the true operational power of a thruster of this class were to be applied (30-50W), the electrodes need to be much more resilient. Further experimentation needs to be conducted and the samples analyzed to see if the same buildup occurs on the AMG as on the CNT samples.

## **3. Plasma Generator and Accelerator Mesh Grid**

The positive lead from the power supply to the plasma generator sees the greatest potential at any given time. Any sharp points or exposed wires/solder can generate an ion plasma cloud outside of the nozzle region of the plasma generator. There is a fair amount of uncertainty as to whether this ion plasma completes any circuit through the baseplate or the negative lead of the power supply (ground) either through the Argon rich atmosphere in the bell jar produced by the exhaust or due to the ion plasma being in close proximity to the copper collector plate. Either way, electrical isolation of the plasma generator and the AMG is paramount to achieve optimal results. A means of neutralizing the exhaust plume may be a desirable addition to the FIEP thruster for future experimentation and later prototyping.

The PCB used for the plasma generator and AMG were a good proof of concept, but the FR4 substrate was insufficient at the voltage required for plasma generation. A simple cheap solution could be a similar design as the PCB, but the ground plane is deposited on a silicon substrate in the NPS MEMS cleanroom. Or, another solution could be the array of CNT nozzles and the PCB are all one electrode.

The plasma generated by the FIEP thruster needs to be characterized further in order to fully understand the electrode dynamics. The first Townsend coefficient corresponding to the field strengths and pressures used should be researched and plotted alongside collected data. This would inform the experimenter what regime of discharge is occurring.

#### **4. Field Ionization Electric Propulsion Geometry**

As discussed in Chapter IV of this thesis, the plasma generator and AMG gap distance was fixed due to the inability to incorporate motors in an ion rich atmosphere. If the plasma exhaust could be neutralized or directed away from any electrical components, a vacuum compatible DC motor like the MFA-CCV6 from Newport could be incorporated into the test apparatus.

#### **5. Characterization of Thrust and Plasma Plume**

Using a MEMS device to measure an ion plasma thrust was never an ideal solution. A mechanical thrust stand that uses either a pressure plate or a LASER to measure deflection would be more suited for this application.

Plasma characterization should both be conducted in the laboratory and in simulation. In the laboratory, spectroscopy could aid in the understanding of the plasma generated by the experimental thruster. Simulation can break down the current being collected and aid in future prototypes. In [11], NASA Jet Propulsion Lab describes the difficulties in characterizing the plume due to the dependence on ambient pressure and the amount of unionized propellant. Simulation is the preferred method for plume characterization.

## APPENDIX A. COMPUTER-AIDED DESIGN

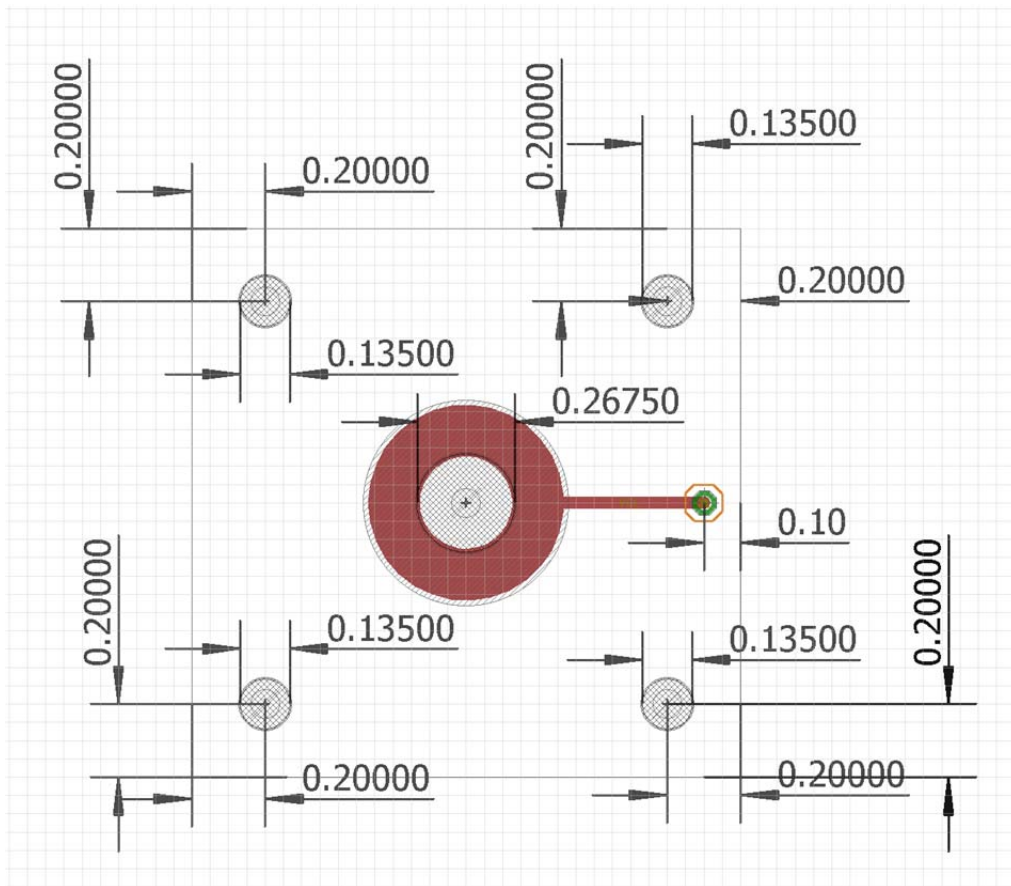


Figure 31. Printed Circuit Board electrode schematic (AutoDesk Eagle Software)

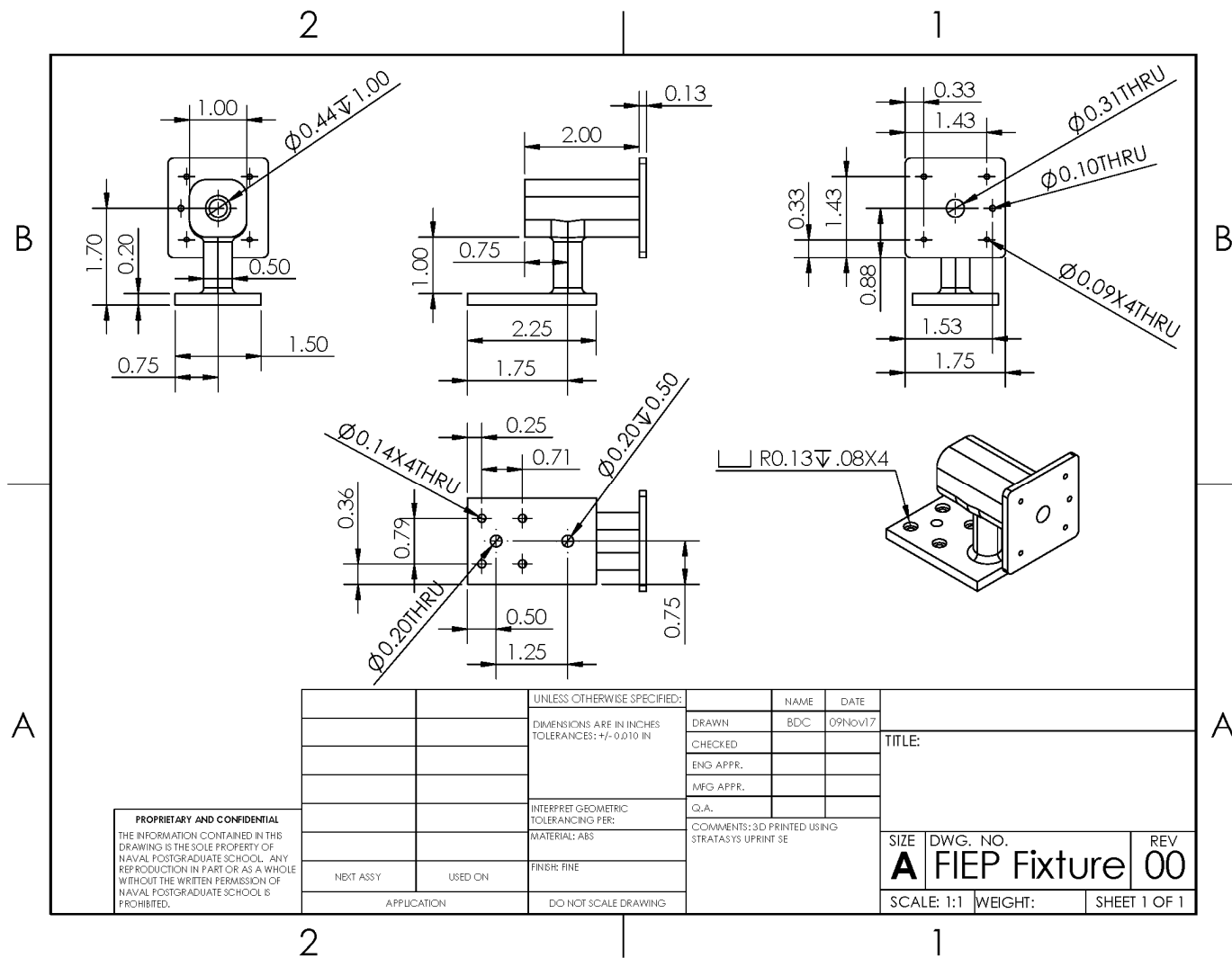


Figure 32. 2D drawing of the 3D printed experimental fixture

## APPENDIX B. RAW THRUST DATA

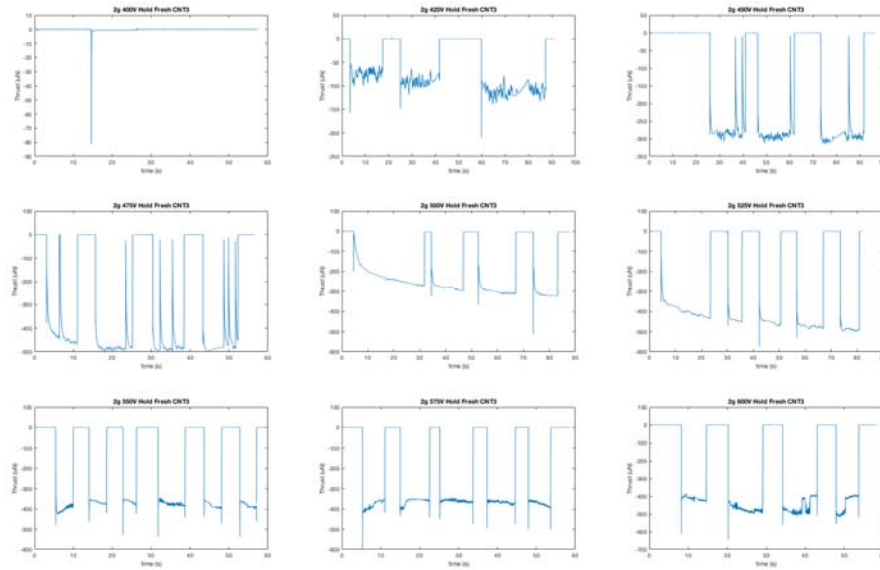


Figure 33. Raw thrust data for a fresh CNT sample at 2g/hr (FT-S1000 Gain: 496.6  $\mu\text{N/V}$ ).

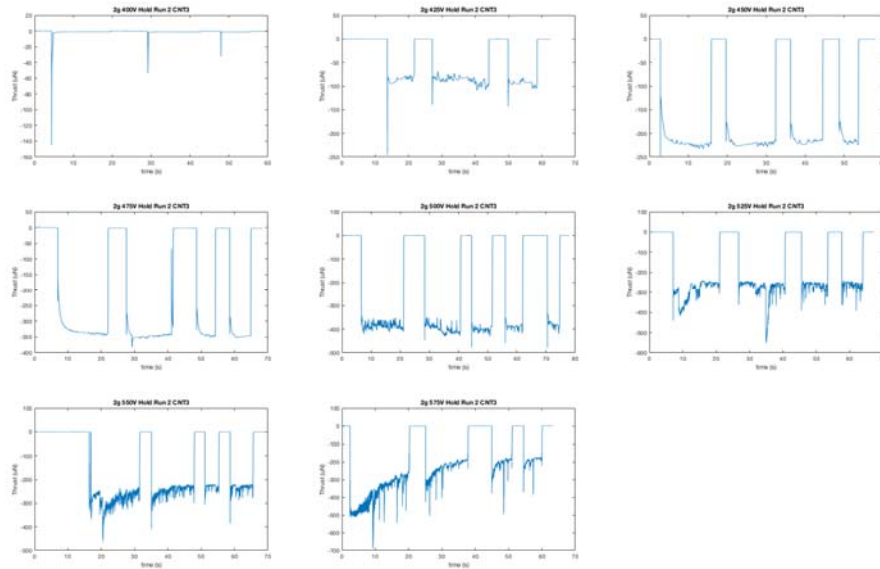


Figure 34. Raw thrust data for the second run of a CNT sample at 2g/hr (FT-S1000 Gain: 496.6  $\mu\text{N/V}$ ).

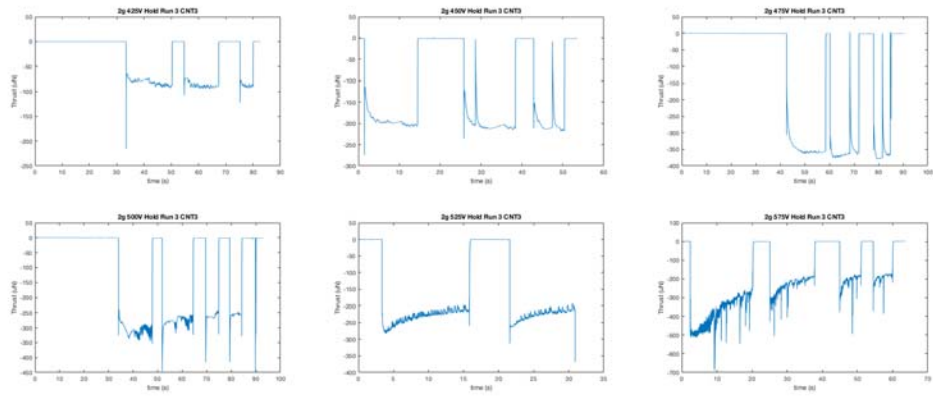
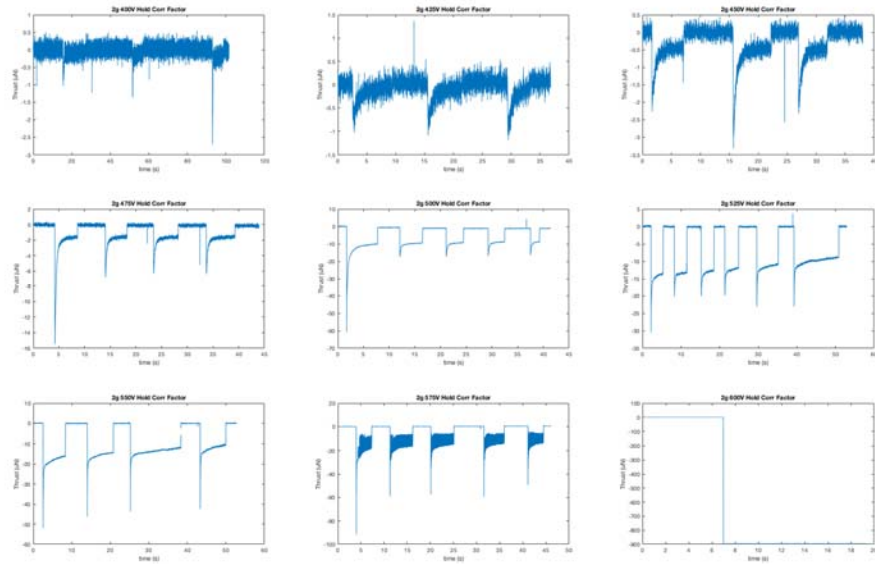


Figure 35. Raw thrust data for the third run of a CNT sample at 2g/hr (FT-S1000 Gain: 496.6  $\mu\text{N/V}$ ).



Correction factor was determined by rotating the force gauge 180 degrees so that the circuitry was in the same location but the cantilever was un-impinged.

Figure 36. Raw thrust data for a correction factor experiment at 2g/hr (FT-S1000 Gain: 496.6  $\mu\text{N/V}$ ).

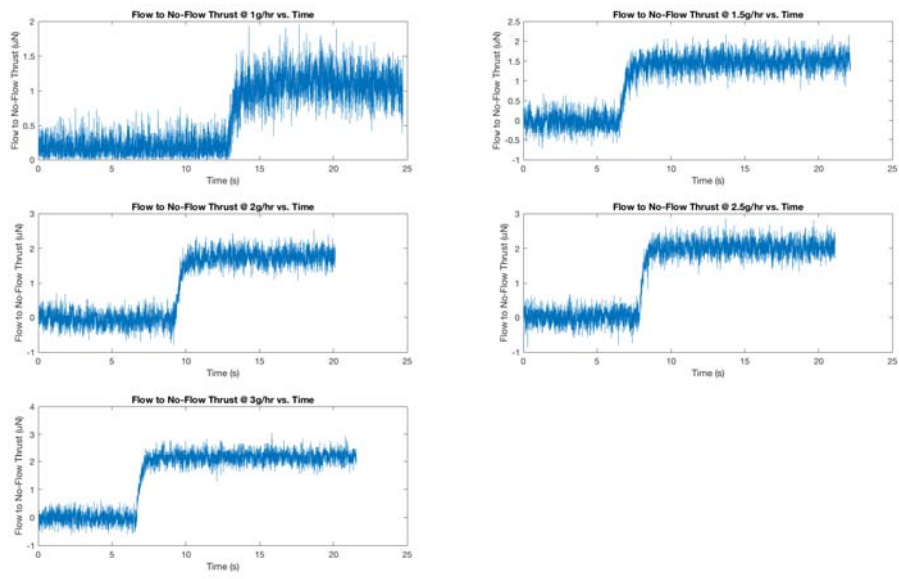


Figure 37. Flow to No-Flow thrust experiments varying mass flow rate (FT-S1000 Gain: 496.6  $\mu\text{N/V}$ ).

THIS PAGE INTENTIONALLY LEFT BLANK

## APPENDIX C. MATLAB CODE

1. Extract and compute the average and standard deviation current corresponding to a constant voltage:

```
function y = FileExtract(File)
% Place this Function in the directory containing .txt files to be read.
dinfo = dir('*.txt');
% Import and extract information on text files from directory hosting the script.
% This will import and parse ALL .txt files in same folder
for k=1:length(dinfo)
    filename = dinfo(k).name; % load data file name
    data{k} = load(filename); % Load this file
    y.Vb(k,1) = data{k}(1,2); % Extract voltage measurements
    Ib{k,1} = data{k}(:,3); % Extract current measurements
    y.Ibm(k,1) = mean(Ib{k,1}); % Average Current Value
    y.Ibs(k,1) = std(Ib{k,1}); % Standard Deviation
end
end
```

2. Extract raw thrust data and time elapsed corresponding to a constant voltage:

```
function y = FileExtract_Thrust(File)
% Place this Function in the directory containing .txt files to be read.
dinfo = dir('*.txt');
% Import and extract information on text files from directory hosting the script.
% This will import and parse ALL .txt files in same folder
for k=1:length(dinfo)
    filename = dinfo(k).name; % load data file name
    data{k} = load(filename); % Load this file
    y.T{k,1} = data{k}(:,2); % Measured Thrust
    y.time{k,1} = data{k}(:,1); % time
end
end
```

3. Compute theoretical values based on collected beam current:

```
function y = expFun(Ib,Vb,Mdot,T)
%Updated 01Sep2017
% Constants
g = 9.807; % Acceleration due to gravity (m/s^2)
e = 1.6022e-19; % Fundamental charge (C)
N = 6.022e23; % Avogadro's # (mol^-1)
eps = 8.85e-12; % Permittivity of Free Space (C^2/Nm^2)~(F/m)
MdotAr = Mdot/(3600*1000); % Converts g/hr to kg/s
PCBd = 6.7945e-3; % Diameter of the PCB Hole
D = 0.0762e-3; % Diameter of mesh grid hole
Holes = PCBd/D; % Number of mesh grid holes in the PCB hole
d = 3.175e-3; % Cathode/Anode gap distance
A = (pi/4)*PCBd^2; % Area of the PCB Hole
Ei = 2.5251e-18; % 1st Ionization Energy of Argon for a single atom (J) (1520.6 KJ/mol)
M = 39.948/1000; % Molar mass of Argon (kg/mol)
vi = 16908.3; % Speed of the initial particle [m/s] - Calculated from Ideal Gas Law
%% Function Arguments
y.Jcl = (4*eps/9)*sqrt(2*e*N/M) .* (Vb.^(3/2))/(d^2); % Child-Langmuir Law
y.k = [(0.5*M/N) .* vi^2]; % Correction coefficient
y.C = (sqrt(y.k)+sqrt(1+y.k))^3; % Correction factor for non-zero initial ion velocity
y.Jmax = y.Jcl*y.C; % Max current density from C-L
y.Ii = MdotAr*e*N/M; % Ideal Current
y.Icl = A*y.Jmax; % Child-Langmuir induced current
y.MUF = Ib.*M/(e*MdotAr*N); % Mass Utilization Factor
y.Vion = sqrt(2*e*Vb/(M/N));
y.Ti = Ib.*sqrt([2*M.*Vb/(e*N)+(M*vi/(e*N))^2]); % Theoretical Thrust from the plasma generator
y.Tcl = y.Icl.*sqrt([2*M.*Vb/(e*N)+(M*vi/(e*N))^2]);
y.Isp = y.Ti./(MdotAr*g); % Specific Impulse
y.P = Ib.*Vb; % Power Consumption
end
```

#### 4. Compute theoretical values based on collected thrust:

```
function y = expFun_Thrust (Ib,Vb,Mdot,T)
%Updated 01Sep2017
% Constants
g = 9.807; % Acceleration due to gravity (m/s^2)
e = 1.6022e-19; % Fundamental charge (C)
N = 6.022e23; % Avogadro's # (mol^-1)
eps = 8.85e-12; % Permittivity of Free Space (C^2/Nm^2)~(F/m)
MdotAr = Mdot/(3600*1000); % Converts g/hr to kg/s
PCBd = 6.7945e-3; % Diameter of the PCB Hole
D = 0.0762e-3; % Diameter of mesh grid hole
Holes = PCBd/D; % Number of mesh grid holes in the PCB hole
d = 3.175e-3; % Cathode/Anode gap distance
A = (pi/4)*PCBd^2; % Area of the PCB Hole
Ei = 2.5251e-18; % 1st Ionization Energy of Argon for a single atom (J) (1520.6 KJ/mol)
M = 39.948/1000; % Molar mass of Argon (kg/mol)
vi = 16908.3; % Speed of the initial particle [m/s]
%% Function Arguments
y.Ii = MdotAr*e*N/M; % Ideal Current
y.MUF = Ib/y.Ii; % Mass Utilization Factor
y.Isp = T./(MdotAr*g); % Specific Impulse
y.Ti = y.Ii.*sqrt([2*M.*Vb/(e*N)+(M*vi/(e*N))^2]).*y.MUF; % Theoretical thrust
end
```

## APPENDIX D. ADDITIONAL IMAGES

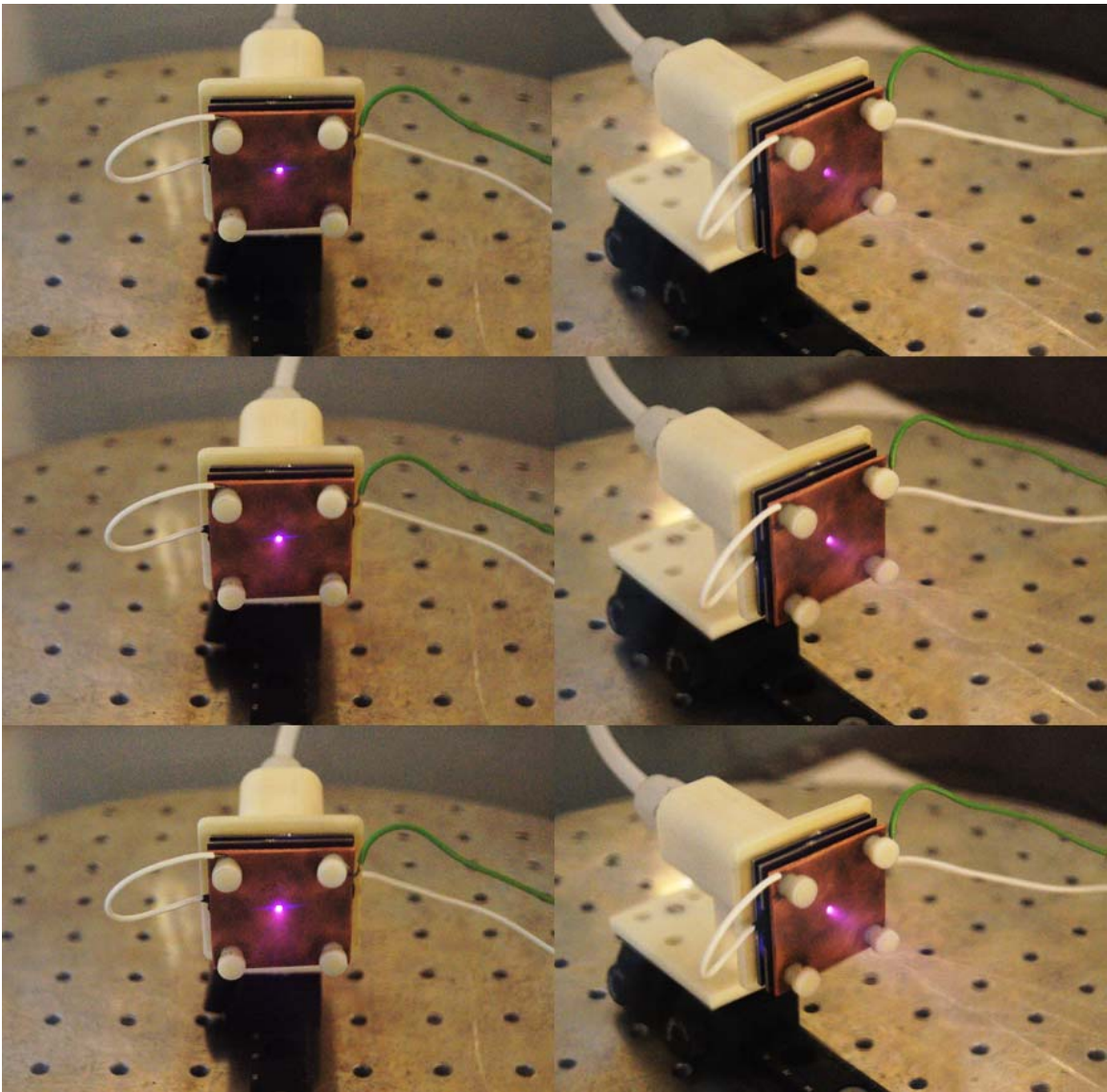


Figure 38. Images showing the relative intensity of the ion plasma from a CNT sample—top: 450V Hold, middle: 500V Hold, bottom: 550V Hold.

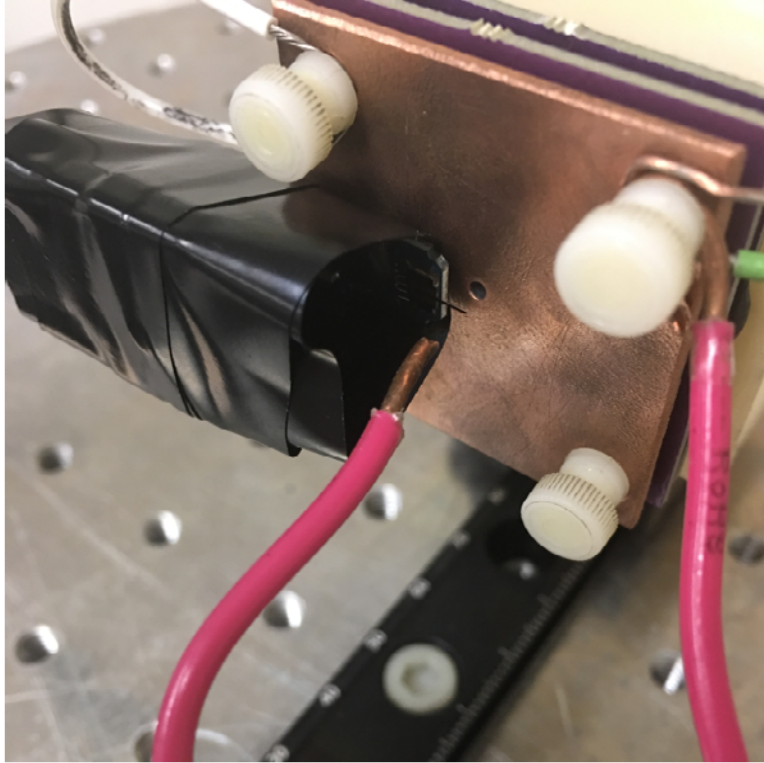


Figure 39. FT-S1000 (Gain:  $496.6 \mu\text{N/V}$ ) cantilever force gauge placement in the plasma plume.

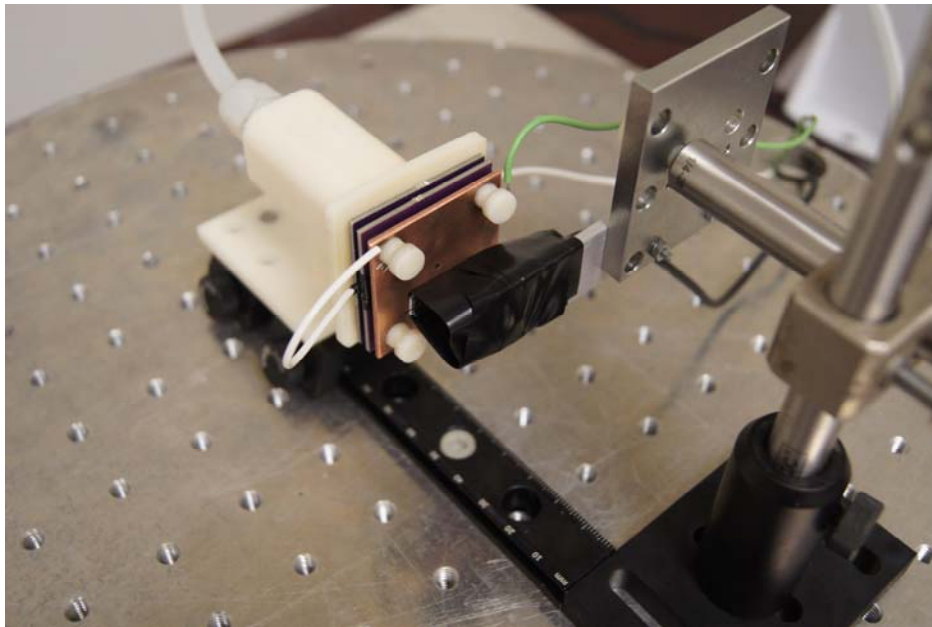


Figure 40. FT-S1000 (Gain:  $496.6 \mu\text{N/V}$ ) cantilever force gauge correction factor experiment.

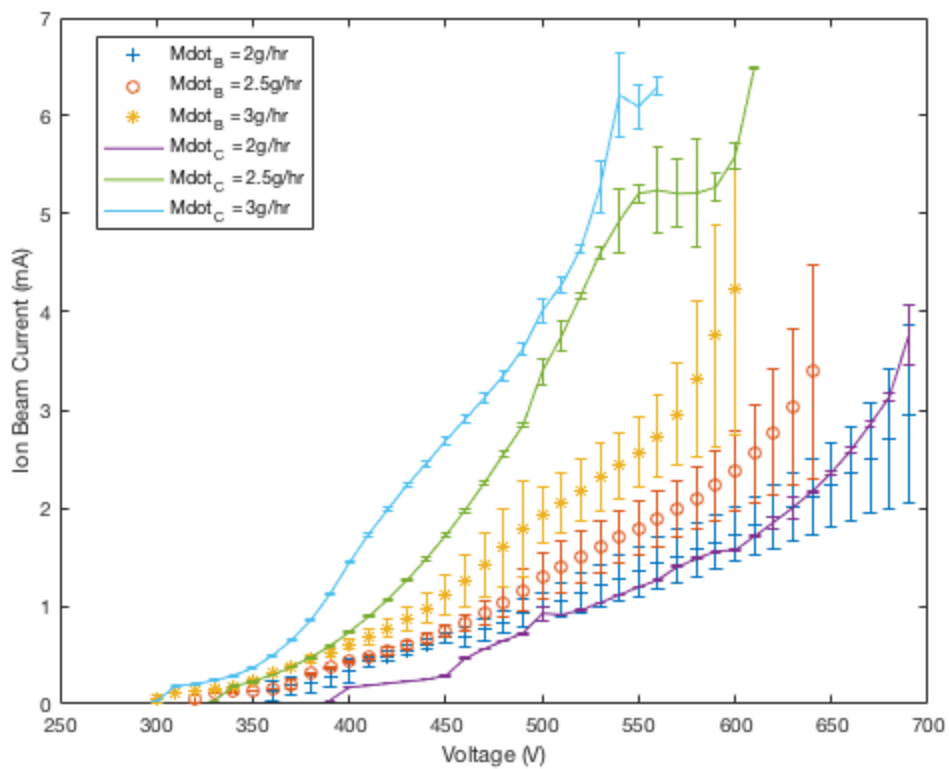


Figure 41. Beam current versus voltage of the Blank sample (average of three experiments) and a fresh CNT sample varying mass flow rate.

THIS PAGE INTENTIONALLY LEFT BLANK



THIS PAGE INTENTIONALLY LEFT BLANK

## LIST OF REFERENCES

- [1] G. P. Sutton and O. Biblarz, Chapter 17 “Electric propulsion,” in *Rocket Propulsion Elements*, 9th ed., Hoboken, NJ, USA: John Wiley & Sons, 2017, pp. 620–670.
- [2] V. Kaushish, “Force limited vibration testing and subsequent redesign of the Naval Postgraduate School CubeSat launcher,” M.S. thesis, Dept. of Mech & Aero. Eng., Naval Postgraduate School, Monterey, CA, USA, 2014.
- [3] M. Leomanni, A. Garulli, A. Giannitrapani and F. Scortecci, “Propulsion options for very low Earth orbit microsattellites,” *Acta Astronautica*, vol. 133, pp. 444–445, April 2017. [Online]. Available: <http://www.sciencedirect.com/science/article/pii/S0094576516305197>
- [4] Accion, Tile-V1 data card. [Online]. Available: <http://www.accion-systems.com/tile/>.
- [5] Busek, Green Monopropellant Thrusters. Accessed November 2, 2017. [Online]. Available: [http://www.busek.com/technologies\\_\\_greenmonoprop.htm](http://www.busek.com/technologies__greenmonoprop.htm).
- [6] Busek, Ion Thrusters Bit-3. Accessed November 2, 2017. [Online]. Available: [http://www.busek.com/technologies\\_\\_ion.htm](http://www.busek.com/technologies__ion.htm).
- [7] Busek, Pulsed Plasma Thrusters BmP-220. Accessed November 2, 2017. [Online]. Available: [http://www.busek.com/technologies\\_\\_ppt.htm](http://www.busek.com/technologies__ppt.htm).
- [8] Phase 4, RFT. Accessed November 2, 2017. [Online]. Available: <http://www.phasefour.io/product/>.
- [9] Vacco, NASA C-POD Micro CubeSat Propulsion System. Accessed November 2, 2017. [Online]. Available: <http://www.cubesat-propulsion.com/reaction-control-propulsion-module/>.
- [10] Fotec, ENPULSION IFM-350. Accessed November 2, 2017. [Online]. Available: <http://www.enpulsion.com/>.
- [11] D. M. Goebel and I. Katz, *Fundamentals of Electric Propulsion Ion and Hall Thrusters*, Hoboken, NJ, USA: John Wiley & Sons, 2008.
- [12] O. Biblarz, “Ion accelerator Currents Beyond the Child-Langmuir Limit”, AIAA Paper 2013-4109, San Jose, CA, Jul. 2013.
- [13] J. J. Hallan, “Carbon nanotube-based field ionization chamber for spacecraft propulsion applications,” M.S. thesis, Dept. of App. Phy., Naval Postgraduate School, Monterey, CA, USA, 2012.

- [14] J. M. Ozereko, "Carbon nanotube enhancement for miniaturized ion thrusters," M.S. thesis, Dept. of App. Phy., Naval Postgraduate School, Monterey, CA, USA, 2015.
- [15] S. Parveen, S. Kumar and M. Husain, "Fowler Nordheim theory of carbon nanotube based field emitters," *Physica B: Condensed Matter*, vol. 505, pp. 1–8, January 2017. [Online]. Available: <http://www.sciencedirect.com/science/article/pii/S0921452616304914>.
- [16] H. D. Beckey, "Field electron emission," in *Principles of Field Ionization and Field Desorption Mass Spectrometry*, Elmsford, NY, USA, Pergamon Press Inc., 1977, pp. 24–25.
- [17] B. L. Crossley, N. E. Glauvitz, B. T. Quinton, R. A. Coutu, Jr. and P. J. Collins, "Characterizing multi-walled carbon nanotube synthesis for field emission applications," in *Carbon nanotubes Applications on Electron Devices*, J. M. Marulanda, Ed. InTech, Rijeka, Croatia, August, 2011.
- [18] C. B. Pace, "Carbon nanotube cathode field emission effect for use with free electron lasers," M.S. thesis, Dept. of App. Phy., Naval Postgraduate School, Monterey, CA, USA, 2014.
- [19] H. D. Beckey, "FI probability," in *Principles of Field Ionization and Field Desorption Mass Spectrometry*, Elmsford, NY, USA, Pergamon Press Inc., 1977, pp. 1–6.
- [20] R. Haydock and D. R. Kingham, "Field ionization theory: A new, analytic, formalism," *Surface Science*, vol. 103, no. 1, pp. 239–247, 1981
- [21] H. D. Beckey, "Minimum distance for FI," in *Principles of Field Ionization and Field Desorption Mass Spectrometry*, Elmsford, NY, USA, Pergamon Press Inc., 1977, pp. 10–16.
- [22] B. Gilbert, "Effect of angled-wall etch design on CNT growth and propellant ionization," M.S. thesis, Dept. of App. Phy., Naval Postgraduate School, Monterey, CA, USA, 2016.
- [23] A. P. Garvey, "Enhanced ionization of propellant through carbon nanotube growth on angled walls," M.S. thesis, Dept. of App. Phy., Naval Postgraduate School, Monterey, CA, USA, 2017.
- [24] P. W. Camp, "Design and installation of a field ionization test chamber for ion thrusters," M.S. thesis, Dept. of Mech. & Aero. Eng., Naval Postgraduate School, Monterey, CA, USA, 2011.
- [25] *Smart-Trak 2 series 100 Mass Flow Meters and Controllers Instruction Manual IM-100-ST2*, Rev. C2, Sierra Inst., USA, 2011.

- [26] F. M. Penning, *Electrical Discharges in Gases*, New York, NY, USA: The Macmillan Co., 1957.
- [27] F. H. Sanders, “The value of the Townsend coefficient for ionization by collision at large plate distances and near atmospheric pressure,” *Physical Review*, vol. 41, pp. 667–677, September 1932. [Online]. Available: <https://journals.aps.org/pr/abstract/10.1103/PhysRev.41.667>.
- [28] J. R. Fiebrandt, “Finite element analysis of particle ionization within carbon nanotube ion micro thrusters,” M.S. thesis, Dept. of App. Phy., Naval Postgraduate School, Monterey, CA, USA, 2017.

THIS PAGE INTENTIONALLY LEFT BLANK

## **INITIAL DISTRIBUTION LIST**

1. Defense Technical Information Center  
Ft. Belvoir, Virginia
2. Dudley Knox Library  
Naval Postgraduate School  
Monterey, California